A highly collateralized thalamic cell type with arousal predicting activity serves as a key hub for graded state transitions in the forebrain

Ferenc Mátyás[#1,2,*], **Gergely Komlósi**[#2], **Ákos Babiczky**[1,2], **Kinga Kocsis**[1,3], **Péter Barthó**[1,2], **Boglárka Barsy**[1,2], **Csaba Dávid**[2,4], **Vivien Kanti**[1,5], **Cesar Porrero**[6], **Aletta Magyar**[1,5], **Iván Sz cs**[7], **Francisco Clasca**[6], and **László Acsády**[2,*]

[1]Institute of Cognitive Neuroscience and Psychology, Research Center for Natural Sciences, Hungarian Academy of Sciences, Budapest, Hungary

[2]Department of Cellular and Network Neurobiology, Institute of Experimental Medicine, Hungarian Academy of Sciences, Budapest, Hungary

[3]Roska Tamás Doctoral School of Sciences and Technology, Faculty of Information Technology and Bionics, Pázmány Péter Catholic University, Budapest, Hungary

[4]Department of Anatomy, Histology, and Embryology, Semmelweis University, Budapest, Hungary

[5]János Szentágothai Doctoral School of Neurosciences, Semmelweis University, Budapest, Hungary

[6]Brain Connectomics Lab, Department of Anatomy and Neuroscience, School of Medicine, Autónoma University, Madrid, Spain

[7]Department of Pathology, Szent Borbála Hospital, Tatabánya, Hungary

[#] These authors contributed equally to this work.

Abstract

Sleep cycles consist of rapid alterations between arousal states including transient perturbation of sleep rhythms, microarousals and full-blown awake states. Here we demonstrate that the calretinin containing (CR+) neurons in the dorsal medial thalamus (DMT) constitute a key diencephalic node that mediates distinct levels of forebrain arousal. Cell-type-specific activation of DMT/CR+ cells could elicit active locomotion lasting for minutes, stereotyped microarousals or transient disruption of sleep rhythms depending on the parameters of the stimulation. State transitions could be induced in both slow-wave and REM sleep. The DMT/CR+ cells displayed elevated activity prior to arousal, received selective subcortical inputs and innervated several forebrain sites via highly branched axons. Together, these features enable DMT/CR+ cells to summate subcortical arousal information and effectively transfer it as a rapid, synchronous signal to several forebrain regions to modulate the level of arousal.

[*]Corresponding authors: Correspondence to László Acsády (acsady.laszlo@koki.mta.hu) and Ferenc Mátyás (matyas.ferenc@ttk.mta.hu).

Introduction

The mechanisms of state transitions during sleep or between sleep and wakefulness are complex and poorly understood[1,2]. Sleep itself is a highly dynamic state which consists of rapid transitions between slow-wave sleep (SWS) and REM sleeps and fluctuating levels of arousal that manifest e.g. as cyclic alternating patterns or microarousals[3–5]. Control of these brain state changes appears to involve an ever-increasing number of interacting brain centers located mainly in the brainstem and the hypothalamus[2,6]. It is still unclear, however, how the final output of these centers is summated and transferred rapidly to the forebrain as a coordinated, graded signal, i.e. how arousal is controlled in a fast and synchronous manner in the forebrain.

Earlier studies using traditional tracing techniques suggested that cells in the dorsal medial thalamus (DMT) receive inputs from the main hypothalamic and brainstem arousal centers and innervate several cortical and subcortical regions in the forebrain[7–10]. DMT utilizes fast glutamatergic transmission[7–9], thus, is in a position to mediate rapid responses in forebrain structures. Indeed, lesions involving DMT in humans have been linked to hypersomnia and altered vigilance states[11,12]. However, thalamic neurons that are functionally related are often not confined to a single nucleus, and thalamocortical cells with distinct properties can intermingle[13]. Moreover, the DMT region includes various nuclei with irregular shape and size, which complicates traditional approaches for anatomical or functional interrogation. As a result, it is still unclear which thalamic neuron population, if any[14,15], mediates forebrain arousal and what neuronal activity governs concerted state changes among forebrain areas.

In both rodents and humans, DMT contains large population of calretinin-positive (CR+) cells scattered across the various nuclei of this region[16,17]. In this study, we tested whether this DMT/CR+ neuronal population plays a specific role in forebrain arousal. Using cell-type specific approaches, we investigated DMT/CR+ neurons' arousal-related activity, connectivity and impact on arousal. We also investigated their inputs in the equivalent human DMT region and compared the properties of arousals elicited by DMT/CR+ cells and sensory thalamic nuclei. Predictive coding before sleep–wake transition, graded arousal responses and widespread, synchronous impact on forebrain targets identified DMT/CR+ cells as a key mediator of forebrain arousal.

Results

Arousal-related activity of DMT/CR+ neurons

Neurons in the DMT are known to display diurnal[18] and stress related[19–23] cFos protein expression. In addition, this thalamic region is known to contain high number of calretinin-containing (CR+) neurons[16]. Thus, to identify whether CR is a reliable marker for the activity-dependent DMT cell population, we perfused mice during the light (Zeitgeber time, ZT2.5, sleep) or the dark (ZT14.5, wake) phase of their diurnal cycles and tested the CR content and cFos expression of DMT cells (Fig. 1a-e). The DMT of mice contained significantly higher number of cFos+ neurons during the dark than in the light phase (Fig. 1b-d, Supplementary Table 1) similar to rats[18]. The vast majority (~91%) of these neurons co-expressed CR in both states (Fig. 1e, Supplementary Table 1). The cFos/CR+ neurons

were present in the major nucleus of the DMT (the paraventricular nucleus, PVN) but were also dispersed in adjacent portions of the anterior intralaminar and mediodorsal nuclei. Since this neuronal population was not confined to a single nucleus, we will refer to it as dorsal medial thalamic calretinin-positive (DMT/CR+) cells throughout this study.

Next, the DMT/CR+ cells were optogenetically tagged using short pulses of blue light (473 nm) in CR (*Calb2*)-Cre mice injected with AAV-DIO-ChR2 (Fig. 1f, g and Supplementary Fig. 1a-d) and their firing were extracellularly monitored during sleep/wake state changes for several hours. Thirty-one out of 65 well-isolated units displayed elevated firing rate to the tagging protocol and were thus considered as CR+ (Fig. 1h, see Methods). The activity of 29 out of these 31 DMT/CR+ cells (93.5%) was correlated with changes in the EMG activity accompanying arousal from sleep. Twenty out of the 31 DMT/CR+ cells (64.5%) started to increase their firing rate significantly up to 5-10 sec prior to the onset of EMG activity and maintained elevated activity for tens of seconds after the EMG activation (labeled as '+/+' cells; Fig. 1h; Supplementary Fig 1g, h). In studies of brainstem neurons, a similar anticipatory elevation of firing rate several seconds prior to EMG activation has been considered as the best indicator for their involvement in arousal[24]. The other eight DMT/CR+ neurons (25.8%) increased their firing at the onset of EMG activity, but not before, and remained active during it (labeled as '0/+' cells; Supplementary Fig. 1e-f). Of the remaining 3 DMT/CR+ cells, one decreased its firing during EMG activation and two showed no changes (labeled as '-/-' and '0/0', respectively; Supplementary Fig. 1h).

Thirty four of the original 65 DMT neurons did not react to the tagging protocol and thus were regarded as putative CR– cells (Fig. 1j). Among these, only 8/34 (23.5%) cells increased their firing prior to EMG activity, while the rest did not (Supplementary Fig. 1i). As a consequence, at the population level, DMT/CR– neurons did not show anticipatory activity in sharp contrast to the DMT/CR+ population (Fig. 1i). Increased firing of DMT/CR– cells at the onset of the EMG signal was also shorter and lasted only for 1-2 sec, not for over 10 sec as in the case of DMT/CR+ cells (Fig. 1j, k). These data show that DMT/CR+ cells selectively display arousal related, predictive firing activity.

To analyze if under arousing conditions during the awake state, such as stress, DMT neurons are also CR+, we subjected three groups of animals to increasingly stressful situations (handling control, habituation to a novel environment (a foot-shock chamber)**[Au:OK?]** and foot shock) before perfusion. The number of cFos+ neurons significantly increased in the DMT in situations eliciting increasingly elevated arousal (Fig. 2a-c, Supplementary Table 1). When tested for CR expression, the vast majority of foot-shock-activated cFos+ cells expressed CR (Fig. 2d, e and Supplementary Fig. 2, Supplementary Table 1).

To assess the response to a painful arousing signal, we measured the firing response of individual, juxtacellularly recorded and labeled DMT/CR+ cells to tail pinch under anesthesia (Supplementary Fig. 3). Tail pinch caused a reduction in the delta power of frontal cortical LFP in all cases. Six out of 13 DMT/CR+ cells significantly increased their activity during tail pinch, and activity remained elevated even after its termination (Supplementary Fig. 3). The remaining cells decreased their firing, which may indicate the existence of an inhibitory signal to DMT[25] that is active during these conditions.

Lastly, to directly examine the role of DMT/CR+ cells during an arousing situation (exploration of a novel environment), we optogenetically silenced them with an inhibitory step-function opsin, SwichR 26 by injecting CR-Cre transgenic mice with AAV-DIO-SwichR-eYFP or AAV-DIO-eYFP (control) and analyzed their locomotor behavior (Fig. 2f). Short pulses (0.5-2 sec) of blue light evoked long lasting inactivation of SwichR-expressing CR+ cells (Supplementary Fig. 4). We found that during the inhibition of DMT/CR+ cells, the number of pauses (lack of movements for time period less than 2 sec) increased by 50% in an open field chamber (Fig. 2g-i) indicating disruption of exploratory activity. Control animals showed no behavioral changes. These data together demonstrate tight links between the activity of DMT/CR+ cells and arousal both at the cellular and behavioral levels.

Graded arousal elicited by DMT/CR+ cells

To directly test whether selective activation of DMT/CR+ neurons can initiate state transitions in freely sleeping animals, first, we checked the reliability of their optogenetic responses (Fig. 3a). CR-Cre mice were injected with AAV-DIO-ChR2-eYFP (Supplementary Fig. 1a-d) and subjected to juxtacellular recording and labeling under urethane anesthesia. When tested with 1 ms laser light, all DMT neurons post-hoc identified as ChR2-eYFP-positve (n = 4 cells) were able to follow 20 Hz stimulation for up to 10 sec with short response latency (1.8 ± 1.1 ms), low jitter and very high probability (0.997 ± 0.005; Fig. 3b-e).

Then, we injected either AAV-DIO-ChR2-eYFP or AAV-DIO-eYFP into the DMT of CR-Cre mice and subsequently photostimulated it with 10 sec long, 10 Hz light pulse trains (see Methods) via a chronically implanted optic fibers, in drug-free conditions (Fig. 3f, g). We used 10 Hz stimulation, since in our freely-moving experiments all recorded DMT/CR+ cells (n = 31) were able to fire at this frequency and 66% of them were able to sustain this activity for at least 1 sec during awakening.

Ten-second activation of DMT/CR+ neurons faithfully induced prolonged behavioral arousal accompanied by active locomotion in all ChR2-injected mice during NREM sleep (Fig. 3h, Supplementary Video 1). Parameters of arousal were measured based on the EMG signal (Supplementary Fig. 5a). Evoked arousal outlasted the stimulation by several minutes (range: 2.17 and 17.89 min; average: 8.9 ± 5.6 min). The photostimulation of DMT/CR+ cells first induced an immediate drop in delta power (Fig. 3h, i) followed by an abrupt increase in EMG activity with a latency of 1.34 ± 0.64 sec (Fig. 3h and Supplementary Fig. 5b). During the first 180 sec following the stimulation, the animals spent 78.66% (141.59 ± 21.43 sec) of their time in active, awake state (EMG ON). The same value for the pre-stimulation period was 3.65%, (6.58 ± 3.54 sec). In the control eYFP injected animals, no arousal was evoked (Fig. 3i; pre-stimulation EMG ON state, 2.07%, 3.72 ± 0.74 sec; post-stimulation EMG ON state 2.87%, 5.17 ± 3.54 sec). These data show that activation of DMT/CR+ cells represents a rapid and strong arousal signal, which results in a prolonged arousal state.

Optogenetic stimulation of DMT/CR+ cells for only 1 sec (10 Hz) induced transient arousals (Fig. 3i). These transient interruptions of sleep, known as microarousals, are considered to be part of the normal sleep behavior both in humans and rodents[3,5,27]. During these events, the animals stayed in their nest and displayed only brief head and neck movements lasting

only for few seconds (3.69 ± 1.31 sec, probability: 0.66 ± 0.19; Fig. 3i, Supplementary Fig. 5c and Supplementary Video 2). The onset of the EMG activity was 2.75 ± 1.48 sec. Similarly to the 10 sec stimulations, EEG delta power dropped sharply; however, in these events it returned to baseline within 30 sec (Fig. 3i). In order to identify whether the primary response to the activation of DMT/CR+ cells was a change in the EEG or a change in the EMG activity, we grouped the responses according to the onset of EMG-ON states and examined the corresponding change in the drop of delta activity. Regardless of the onset of the EMG activity, the onset of the change in delta power was instantaneous and preceded the corresponding EMG change (Supplementary Fig. 6a-b). In addition, measurement of time differences between the onset of reduction in delta power and the onset of EMG activity in individual arousal events demonstrated that the primary response following DMT/CR+ activation is a cortical arousal followed by a change in muscle activity (Supplementary Fig. 6c). These observations argues for a top-down cortical effect on behavior not for a direct action of DMT/CR+ cells on motor centers.

Next, we examined the transitions between micro- and prolonged arousals using various stimulus durations (0.5, 1, 2 and 10 sec) but the same laser power during NREM sleep. The probability of arousal increased with increasing stimulus duration (Fig. 3j). The mean durations of evoked EMG ON states in the first 60 sec following stimulus onset also increased with longer stimuli (Fig. 3k top and 3l, Supplementary Fig. 5c). The average duration of microarousals evoked by 1 sec long stimulations did not differ from the duration of spontaneous microarousals, recorded in control periods (Fig. 3k bottom).This indicates that the 1 sec optical stimulations evoked a behaviorally relevant arousal pattern. Together, these data show that graded recruitment of DMT/CR+ cells elicits distinct, graded natural arousal patterns.

We also examined if any alterations in cortical EEG can be observed in those cases when the 1 sec photostimulation of DMT/CR+ cells did not induce arousal as detected by EMG activity (i.e. "sleep-throughs"28) (Fig. 3m-q). We compared changes in delta and sigma powers following the stimulations that resulted in microarousals or sleep-throughs. A sharp drop in delta power with comparable size could be observed both in microarousals and sleep-throughs. However, this perturbation recovered much faster in case of sleep-throughs than microarousals (see Method; Fig. 3m-o). A large drop in sigma power with comparable size was also evident in both microarousals and sleep-throughs, but, in contrast to delta, sigma power returned to baseline slowly in both cases (Fig. 3p, q). These data indicate that, even in the absence of overt behavioral (EMG) activity, activation of DMT/CR+ cells can disrupt ongoing sleep oscillations and, thus, can induce cortical arousal. The extent of this perturbation is different in the two main frequency bands of NREM sleep.

Finally, in order to determine if cortical states differ in case of stimulations resulting in microarousals versus stimulations resulting in sleep-throughs, we compared the cortical evoked responses after DMT/CR+ stimulations in these two cases, but found no difference (Supplementary Fig. 7a). We also examined the EEG powers preceding the laser activation (Supplementary Fig. 7b, c). Pre-stimulation power values up to 40 seconds before the laser activation did not differ between sleep-throughs and microarousals in the delta and sigma bands. These data show that failure of EMG activation following EEG changes in cases of

sleep-throughs is not the consequence of overt differences in cortical states or receptivity to DMT/CR+ activation, but rather a result of the variable efficacy of cortical arousal over the motor responses.

State transitions during REM sleep

Microarousals are also prevalent at the REM–NREM state transitions. In our recording conditions, mice expressed higher spontaneous rate of microarousals during (or after) REM than during NREM sleep (0.012 ± 0.003 Hz, vs. 0.007 ± 0.001 Hz respectively, n = 8 mice, two-tailed paired t-test, t(7) = -5.451, p = 0.0009). The duration of REM-linked microarousals were significantly longer (7.19 ± 4.4 sec for REM vs, 3.23 ± 1.27 sec for NREM, n=8, two-tailed paired t-test, t(7) = 2.576, p = 0.037). In most of the cases, the animals returned to NREM following REM linked microarousals.

One-second photostimulation of DMT/CR+ cells during REM sleep evoked microarousals in 4 out of the 6 animals, with an average probability of 0.57 ± 0.21 (n = 4) (Fig. 3m-o). Duration of evoked microarousals during REM was longer than during NREM (5.41 ± 2.34 sec vs 3.03 ± 0.75 sec, n=4, two-tailed paired t-test, t(3) = 2.82, p = 0.067), mimicking the spontaneous condition. Following evoked microarousals during REM, animals switched to NREM sleep as shown by a gradual increase of delta power (Fig. 3o bottom). This activity pattern recapitulated the spontaneous REM–microarousal–NREM transitions.

These data together demonstrate that graded activation of DMT/CR+ neurons is able to evoke distinct, behaviorally relevant arousal patterns such as full-blown persistent arousal, microarousals, subthreshold disruption of sleep rhythms, as well as state transitions from SWS-to-wake and REM-to-SWS.

Distinct arousal via DMT/CR+ and sensory nuclei

Arousal from sleep may occur spontaneously, in the absence of any particular sensory stimuli, or as a result of certain sensory stimulation (e.g. tactile or acoustic). In order to compare these two types of arousals under similar experimental conditions, we optogenetically activated the ventrobasal complex (VB), which contains the main somatosensory relay nuclei of the thalamus. We injected Syn-AAV-ChR2 into VB of CR-Cre mice and applied unilateral photostimulation with the 1 sec 10 Hz stimulation protocol (Fig. 4a-c). VB stimulation evoked microarousals in NREM sleep with high probability (Fig. 4c-f; Supplementary Fig. 7.d). Microarousals evoked by VB had longer durations (VB, n = 7 mice, 4.55 ± 0.3 sec vs. DMT, n = 6 mice, 3.69 ± 1.31 sec; 2*one-tailed Mann-Whitney, p = 0.029) and shorter latencies (VB, 0.36 ± 0.28 sec vs. DMT: 2.72 ± 1.43; 2*one-tailed Mann-Whitney, p = 0.0003). However, in contrast to DMT/CR+ stimulation, VB stimulations were ineffective during REM sleep (Fig. 4d-f) indicating a qualitative difference between the two conditions. During NREM sleep, the VB stimulations that did not result in EMG activation (i.e. in sleep-throughs) also evoked transient changes in case of sigma powers (Supplementary Fig. 7. e-f).

In order to study how microarousal properties depend on graded parameters of photostimulation, we established intensity/response curves for both DMT/CR+ and VB stimulations by using different laser intensities and plotting arousal probabilities, latencies

and durations. In both groups, the probability of evoked microarousals during NREM sleep displayed graded responses that correlated positively with the laser intensities and could be fitted by a sigmoid function (Fig. 4g and Supplementary Fig. 8a, b). We observed a significant negative correlation between laser intensities and microarousal latencies in VB but not in DMT/CR+ stimulations (Fig. 4h). Similarly, the applied laser intensities correlated with the duration of microarousals only in VB but not in DMT/CR+ cases (Fig. 4i). This indicates that the exact properties of VB microarousals depend much more on stimulus strength, suggesting that external, sensory signals may evoke microarousals in 'dose-dependent' manner. In contrast, arousal patterns evoked by DMT/CR+ cells seem to be more stereotyped: after reaching a threshold, the behavioral outcome did not depend on the size of the recruited DMT/CR+ population.

Widespread, effective forebrain outputs

Next, we tested whether DMT/CR+ cells have the necessary connectivity and sufficiently strong and synchronous impact on their targets that could support a generalized function like arousal. By mapping the axons of AAV-DIO-ChR2-eYFP infected DMT/CR+ cells, we found that these cells provided widespread projection to extensive cortical as well as subcortical forebrain targets (Fig. 5a-j and Supplementary Fig. 9a-k). We observed profuse axon arborizations in several layers of the prelimbic (PrL), insular, perirhinal and entorhinal cortices as well as in the subiculum. In addition layer 6 of almost every cortical regions were innervated at a lower density. Rich innervation reached the core and shell of nucleus accumbens (NAc), the olfactory tubercle, the basolateral and central amygdala (AMY) and the lateral septum. In addition, the hypothalamus, the dorsal striatum and the bed nucleus of stria terminalis also received significant amount of DMT/CR+ fibers.

Next, we tested to what extent the DMT/CR+ cells are responsible for the thalamic inputs to these regions in the case of three main forebrain targets[8,9]. We found that 95-98 % of the retrogradely labeled neurons from PrL, Amy and NAc displayed CR immunoreactivity (Supplementary Fig. 9l-n; Supplementary Table 2), indicating that the CR+ cells provide the vast majority of the total DMT inputs to these forebrain sites.

To assess the impact of DMT/CR+ cells on their targets we simultaneously recorded in vivo multiunit activity in the PrL, the AMY and the NAc while optical stimulation was delivered to DMT under urethane anesthesia, following AAV-DIO-ChR2-eYFP injection into the DMT of CR-Cre mice. One Hz stimulation reliably activated neurons in all three postsynaptic targets with fast onset (<10ms), consistent with a monosynaptic glutamatergic pathway (Fig. 5k-n). Ten Hz stimulation was still effective in driving the targets and did not cause a delay in the timing of response (Fig. 5o-t). The magnitude of the response depended on stimulus intensity. The multiunit and cortical LFP signal displayed depression at 10 Hz (Supplementary Fig. 10a-d). These data show that DMT/CR+ have widespread projections and can effectively drive their main cortical and subcortical targets.

To find out whether these widespread signals are broadcasted by highly collateralized DMT/CR+ cells or rather by separate populations which project to distinct regions, we utilized three methods which assessed the extent of DMT/CR+ collateralization among multiple target regions. Dual injections of retrograde tracers to PrL-AMY, PrL-NAc, and

AMY-NAc resulted in 7-30% of dual labeled cells (Fig. 6a-c and Supplementary Fig. 11a-l, Supplementary Table 3) confirming earlier results in rat 29,30. Dual retrograde tracing is, however, known to grossly underestimate neurons with branching axons. Thus, we labeled isolated DMT/CR+ neurons in 7 mice (9 neurons) with an RNA construct (Pal-eGFP-Sindbis). This method resulted in individual axon arbors branching to reach multiple targets in every cases (Supplementary Fig. 11m-o and Supplementary Table 4). Neurons projecting to more than one target (among PrL, AMY and NAc) were exceedingly rare in other brain regions (Supplementary Fig 11q-r).

Finally, in order to quantify the amount of DMT/CR+ fibers in one target area which derives from neurons projecting to another, we utilized a quantitative retro-anterograde tracing method (also called collateral labeling31) using the AAV-DIO-ChR2-eYFP virus in the CR-Cre animal (See Methods). We systematically examined the collateralization DMT/CR+ cells projecting to PrL (Fig. 6d-f). First, we measured the length of axon arbor in PrL resulting from direct anterograde labeling of the DMT/CR+, thalamo-PrL pathway in a 100 micrometer-wide cortical slab (11389 ± 1000 mm, Fig. 6g). Next, we measured what proportion of these PrL axons originate from neurons that simultaneously project to other targets. Injecting the same AAV vector into NAc, following retro-anterograde transport of the virus, the amount of fibers in PrL was 70 ± 4 % (7956 ± 475 mm; Fig. 6g) of the direct DMT→PrL anterograde labeling. These data clearly show that the vast majority of DMT/CR+ axons in PrL are arising from cells which also project to NAc. The same retro-anterograde approach applied to AMY labeled 32 ± 11 % (3637 ± 1633 mm) of the total anterograde fiber length in PrL (Fig. 6f, g) indicating less widespread but still significant collateralization among these two targets.

In order to test the efficacy of these branching axons to drive postsynaptic targets we used "antidromic–orthodromic" experiments (see Methods), assuming that antidromic spikes evoked in one part of the axon arbor will invade axon branches targeting another region in an orthodromic manner. Thus, we optogenetically activated DMT/CR+ fibers in NAc and recorded the evoked multiunit activity (MUA) in PrL (Fig. 6h). These experiments measured whether DMT/CR+ cells that have collaterals in NAc are able to drive the activity of their PrL target cells. Indeed, "antidromic–orthodromic" activation successfully evoked elevated MUA in PrL with short latency (<10 ms) (Fig. 6i). Reliable "antidromic–orthodromic" MUA responses could also be evoked in BLA after NAc stimulation (Fig. 6i, j). Only minor antidromic–orthodromic responses could be detected on the contralateral PrL (Fig. 6i) after NAc stimulations, confirming low abundance of interhemispheric collateralization (Supplementary Table 4). "Antidromic–orthodromic" MUA had similar latency to the orthodromically evoked MUA both in PrL and BLA. These data show that single DMT/CR+ neurons axons target and able to simultaneously drive multiple forebrain regions. Such cellular features are optimal to elicit a generalized, brain wide effect like arousal.

Selective inputs of DMT/CR+ in mice and humans

To provide arousal-specific inputs to the forebrain, DMT/CR+ cells might be expected to receive selective inputs from subcortical cell networks. DMT is known to be contacted by many hypothalamic and brainstem afferents7–9 some of which contain glutamate32 or

orexin6. Both of these substances play a role in arousal6,33. Thus, as a representative example, here we examined the association of these two major subcortical input systems (the orexinergic and glutamatergic) and the DMT/CR+ cells in mice and for comparisons in humans.

In mice thalami, orexin-immunopositive fibers provided a highly selective innervation of DMT/CR+ cells irrespective of the exact nuclear position (Fig. 7a-c). CR+ cells located both in the paraventricular nucleus as well as those scattered in the rostral intralaminar nuclei received dense orexinergic inputs, whereas nearby DMT regions were devoid of orexin-positive fibers. Similar observations were made in case of subcortical, glumatatergic terminals labeled by vesicular glutamate transporter 2 (vGLUT2)34 (Fig. 7d-f).

In order to study the DMT/CR+ system in humans and its selective subcortical innervation, we performed parallel experiments in postmortem human tissue In humans (n=4), CR+ cells were distributed along the ventricular wall of the thalamus35,36 (Fig. 7g-l). Like in mice, a substantial number of CR+ cells were also distributed in the intralaminar nuclei. Irrespective of the shape or size of DMT/CR+ region in humans, orexinergic axon terminals selectively innervated the CR+ cell groups (Fig. 7g-i) in a pattern similar to that observed in mice. Like in mice, heat maps of vGLUT2 fiber density displayed high values in midline and intralaminar regions in correspondence with the distribution of DMT/CR+ cells, whereas the adjacent regions of the mediodorsal nucleus were practically free of any vGLUT2-positive axons, demonstrating highly selective innervation of the DMT/CR+ cells (Fig. 7j-l).

Discussion

In this study, we demonstrated several features of DMT/CR+ neurons which identify them as a key thalamic cell population controlling spontaneous forebrain arousal. DMT/CR+ cells received selective subcortical inputs and provided widely branching, effective, glutamatergic outputs to several major forebrain centers. In freely sleeping conditions DMT/CR+ cells displayed anticipatory, arousal-related activity several seconds before spontaneous behavioral arousal, a major feature of neurons involved in state changes24. Their optogenetic manipulations were able to bi-directionally modulate arousal levels. Graded activation of DMT/CR+ neurons evoked biologically relevant graded arousal patterns and state transitions (sleep-throughs, microarousals, persistent arousals) which were qualitatively different from arousal elicited by activation of a sensory system. Based on these data, we propose that DMT/CR+ cells represent a highly specialized neuronal hub, which is able to summate and simultaneously transfer brainstem arousal signals to a wide array of subcortical and cortical forebrain structures.

Behavioral patterns elicited by DMT/CR+ cells were biologically relevant. Evoked NREM microarousals were indistinguishable from spontaneous microarousals. Evoked REM microarousals were longer than evoked NREM microarousals, like in the spontaneous condition, and the sequence of state changes induced during REM sleep (REM-microarousal-SWS sequence) also mimicked the natural pattern. Long (10 sec) stimulation evoked prolonged, active locomotion for up to tens of minutes, similar to spontaneous arousals which can be observed at the end of the sleep phase.

The connectivity of DMT/CR+ cells was highly specialized and distinct from that of DMT/CR– cells. DMT/CR+ cells received selective subcortical inputs both in mice and humans. The similarities in two mammalian species that diverged over 80 million years ago are consistent with an evolutionary ancient role for by DMT/CR+ cells in relaying arousal-related information from subcortical centers to the forebrain. Furthermore it supports the notion that CR content, rather than its location in a specific thalamic nucleus,[Au:OK?] is the key trait for anatomically defining this system. The highly collateralized output of DMT/CR+ cell could simultaneously activate several forebrain regions. Our antidromic–orthodromic experiments unambiguously demonstrated that axon potentials elicited by optogenetic activation of the axon arbor in one brain regions will invade collaterals that innervate other regions, hence this method is useful tool to assess collateralization.

The DMT/CR+ elicited arousals always followed a fixed sequence of events. Disruption of EEG rhythms (i.e. cortical arousal) was the first and instantaneous response. This can be attributed to the strong and widespread activation of the postsynaptic forebrain targets with short response latencies (below 10 ms) via the highly collateralized efferent connectivities of these cells. Both delta- and sigma-band activity displayed a sharp drop after stimulation. When delta activity returned to baseline with fast kinetics, no behavioral response could be observed (sleep-through). However, if delta activity remained low, EMG activity — i.e. behavioral arousal — ensued with a delay 2-3 sec. These data clearly dissociated the electrophysiological and motor components of the arousal (EEG and EMG). The observed EMG changes are likely the consequence of a multisynaptic37 top-down influence of the aroused forebrain on brainstem motor centers rather than resulting from direct DMT action on muscle activity, for the following reasons: i) the altered EEG activity following DMT/CR+ activation always preceded the change in EMG activity; ii) DMT/CR+ activation was able to alter EEG activity even in the absence of EMG arousal (sleep-throughs); iii) DMT/CR+ cells did not have direct descending collaterals to brainstem motor centers. Shorter EMG arousal onset was observed after VB stimulations, which may indicate a different routes to motor responses38 in another arousal system.

Brief DMT stimulations qualitatively changed arousal responses from persistent to microarousals. In case of these short stimulations, stronger laser intensities (i.e. recruiting more DMT/CR+ neurons) could evoke microarousals with higher probability, but these activations never resulted in prolonged arousal. This indicates that DMT/CR+ neurons may constitute a crucial filter to protect sleep integrity against brief, random increases in brainstem activity during sleep.

In the absence of microarousals, activation of DMT/CR+ cells could still perturb ongoing sleep oscillations. During these subthreshold responses, the two major sleep rhythms (delta and sigma) displayed distinct sensitivity to the thalamic activation. Sleep spindles were more sensitive to perturbations, probably due to the highly intricate network mechanism responsible for their generation, whereas the more robust, globally generated delta activity was more resistant. However, when delta activity was perturbed for longer duration, it was tightly linked to altered EMG activity.

Our data together demonstrate that graded recruitment of DMT/CR+ cells determines a precise behavioral outcome and suggest that the variable optogenetic stimulation we used here imitate the graded activation of DMT/CR+ cells during arousal. Indeed, the increased spontaneous activity of optically tagged DMT/CR+ (but not DMT/CR–) cells anticipated the onset of EMG activity in animals arousing from sleep by several seconds, which to our knowledge has not been described in the forebrain.

DMT has been proposed to play important role in arousal in earlier papers[39,40]. This idea, however, was criticized later, due to the artifacts of electrical stimulation used in the original experiments, and almost entirely abandoned [14,41,42]. Recent investigations have linked the DMT nuclei to wide range of brain functions including fear learning[22,23,43], reward[44–46], feeding behavior[47,48], social interactions[49]. Our present data demonstrate that besides the above specific functions, the highly collateralized DMT/CR+ neurons are involved in arousal, which is a necessary component for the active execution of any given behavior[50]. It should also be noted that although the above mentioned studies ascribed various roles to specific DMT pathways (e.g. DMT-AMY or DMT-NAc), our present data demonstrate that DMT neurons projecting to a single target are exceedingly rare, if they exist at all. The differences between DMT/CR+ and DMT/CR– in terms of connectivity, activity and cFos expression clearly indicate that it is the cell's phenotype rather than its localization in a particular thalamic nucleus[13] **[Au:OK?]** that is the critical variable in DMT neuronal functions, underlining the importance of cell-type specific approach in DMT. Whether within the DMT/CR+ neurons specialized and generalized roles are linked to the same or different neuronal sub-populations remains to be established.

Methods

Experimental models

Adult (> 2 months of age) CR-(*Calb2*)-Cre (a gift from Z. Josh Huang) and CBA/Bl6J mice from both sexes were used for the experiments. Female mice were used only in case of the anatomical experiments. They were group housed of 3-5 mice in transparent Plexiglass cages (367 x 140 x 207 mm) in a humidity- and temperature-controlled environment. During testing, mice were kept individually. Mice were entrained to a 12 h light/dark cycle (light phase from 7:00) with food and water available ad libitum. Testing occurred in the light phase.

Control human thalamic tissues (n=4) were obtained from a male subjects (55-77 years old) who died from causes not linked to brain diseases. None of them had a history of neurological disorders. The four subjects were processed for autopsy in the Department of Pathology, Szent Borbála Hospital, Tatabánya, Hungary. Informed consent was obtained for the use of brain tissue and for access to medical records for research purposes. Tissue was obtained and used in a manner compliant with the Declaration of Helsinki.

All procedures were approved by the Regional and Institutional Committee of Science of Experimental Medicine of the Hungarian Academy of Sciences, Research Centre for Natural Sciences and the Autonoma University in Madrid and Research Ethics of Scientific Council

of Health (ETT TUKEB 31443/2011/EKU (518/PI/11)). The experiments were approved by the National Animal Research Authorities of Hungary and Spain.

Viral injection

AAV2/5-Ef1a-DIO-ChR2-eYFP, AAV2/5-Ef1a-DIO-SwichRCA-eYFP, AAV2/5-Ef1a-DIO-eYFP viruses (50–100 nl; Penn Cector Core or UNC; titer: $5x10^{12}$-$1x10^{13}$ GC/mL) were injected at a rate of 1 nl/sec into the dorsal medial thalamus (DMT, AP -0.9 to 1.1, ML 0, DV 2.8 –3.2 mm from the brain surface) or into a target region: prelimbic cortex (PrL, AP 2, ML 0.3, DV 2 mm), nucleus accumbens (NAc; AP 1.4, ML 0.8, DV 4 mm) and amygdala (AMY, AP -1.5, ML 3.3, DV 4 mm). For anatomical analysis, after 3-8 weeks of survival time, mice were perfused first with saline, then, with ~150 ml of fixative solution containing 4% PFA in 0.1 M phosphate buffer (PB). Tissue blocks were cut on a Vibratome (Leica) into 50 μm coronal sections and fluorescently counterstained for parvalbumin (PV; rabbit, Swant: PV27; 1:3000), calretinin (CR; mouse, Swant: 6B3; 1:1-3000), choline acetyltransferase (Chat 51; mouse, 1:500) and Orexin (Orx; goat, Santa Cruz: sc-8071; 1:2-5000) with a secondary antibodies conjugated with a fluorescent IgGs (Alexa488-donkey anti-mouse IgG (H+L), Jackson ImmunoResearch, 715-545-150; Alexa488-donkey anti-rabbit IgG (H+L), Molecular Probes, A21206; Alexa488-donkey anti-goat IgG (H+L), Molecular Probes, A11055; CY3-donkey anti-rabbit IgG (H+L), Jackson ImmunoResearch, 711-165-152; CY3-donkey anti-mouse IgG (H+L), Jackson ImmunoResearch, 715-165-151; Cy3-donkey anti-goat IgG (H+L), Jackson ImmunoResearch, 705-165-147; Alexa647-donkey anti-mouse IgG (H+L); Jackson ImmunoResearch, 715-605-151) to identify the DMT-targeted cortical and subcortical regions.

In vivo electrophysiology in anesthetized preparations

In vivo recordings were performed 4–8 weeks after the viral injections. For LFP recordings, 16-channel silicon probes were lowered in the PrL (AP +2, ML 2.5, DV 3.5 mm at 55 degrees) and primary somatosensory cortex (S1; AP 1.2; ML 3.2 and DV 1.2 mm at 20 degrees). Thalamic, ventral striatal and amygdalar multiunit activities (MUA) were monitored via 32-channel linear silicon probes (Neuronexus) labeled by DiI. Two different recording conditions were utilized. First, the optic fibers were lowered to DMT and classical orthodromic responses were recorded. Next, the optic fibers were repositioned to the NAc and fibers of DMT/CR+ were activated and the evoked MUA (eMUA) responses were detected in PrL and AMY. Under this latter conditions, action potentials first traveled antidromically and at a putative branching they could turn to orthodromic direction as well, hence we call this "antidromic-orthodromic" activation. Since NAc contain no CR+ cells, NAc projecting neurons are GABAergic and they do not project to PrL, fast activation of PrL neurons is only possible via the branching collaterals of DMT/CR+ cells.

Silicon probe signals were high-passed filtered (0.3 Hz), amplified (2000X) by a 256-channel amplifier, and digitized at 20 kHz (Intan Technologies). Single-unit activity was recorded by glass microelectrodes (in vivo impedance of 10 – 40 MD) filled with 0.5 M NaCl and 2% neurobiotin (Vector Laboratories). Neuronal signals were amplified by a DC amplifier (Axoclamp 2B, Molecular Devices), further amplified and filtered between 0.16 and 5 kHz by a signal conditioner (LinearAmp, Supertech). Optogenetic tagging in AAV2/5-

EF1a-DIO-ChR2-eYFP injected animals was done with 473 nm light pulses (1 ms; 1 Hz; 10 mW). Juxtacellular labeling of the recorded neurons was performed 52. Latency of evoked AP was calculated as time-to-peak, while spike fidelity as proportion of evoked AP. Tail pinch (30 s) as an arousal signal was applied.

After recordings, animals were transcardially perfused and coronal sections were cut. The labeled cells were visualized with streptavidin-conjugated fluorescent immunoglobulin tagged with a fluorescent protein (Cy3 or Alexa-488; in 1:2000 for 2h at room temperature) or avidin-biotin complex (Vector Laboratories; 1:300, 2 h) developed by nickel-intensified diaminobenzidine, as a chromogen. Identifying the phenotype of the recorded cells, anti-CR fluorescent counterstaining was performed using mouse or rabbit anti-CR antibody (SWANT, 6B3/7697, 1:3000, overnight at room temperature) and with Cy3-(Jackson ImmunoResearch Laboratories) or Alexa- 488-conjugated anti-mouse secondary antibody (Invitrogen) (1:500; 2 h at room temperature). The position of the silicon probes were verified by DiI labeling of the tissue along the electrode track.

Polysomnographic experiments

Surgeries for combined electroencephalography (EEG)/electromyographic (EMG) recordings and optogenetic stimulation were performed on adult male CR-Cre mice at least 4 weeks after viral injection of AAV2/5-EF1a-DIO-ChR2-eYFP or control EF1a-DIO-eYFP into DMT (AP -1.0, ML 0, DV 2.8-3.2 mm), or AAV2/5-hSyn-ChR2-EYFP into VB (AP -1.7, ML ±1.7, DV 3.4 mm). Screw electrodes were implanted into the skull (frontal screws: AP +2, ML ± 2 mm; parietal screws: AP -1.2, ML ± 3 mm); the ground and reference screw electrodes were placed above the occipital bone and the multimode optic fiber (105 nm core diameter, NA = 0.22, Thorlabs) was lowered into DMT (with 10 degrees angle to avoid the superior sagittal sinus) or VPM. The screws and optic fibers were secured to the skull by multiple layers of dental acrylic (Heraeus Kulzer). Mice were allowed at least 10 days to recover.

During recordings, animals were left in their home cage to sleep during light phase (between 8 am and 8 pm). The vast majority of stimulations (80%) occurred between 12.30 and 16.30 i.e in the second half of the light phase. After each experiment, mice were left to rest in the subsequent two days (at least). The signals were recorded amplified and digitized at 20 KHz (KJU-1001, Ampliplex).

Optogenetic stimulation of DMT or unilateral VB was carried out using 5 ms pulses of 473 nm laser (LaserGlow) at varying intensities (0.001-46 mW) and frequencies (1-20 Hz) for 0.5-10 sec via a data acquisition board (National Instruments) controlled by custom-built MATLAB programs. The values for individual animals are shown in Supplementary Fig. 8. In order to obtain comparable data the laser power used in each animal was set to obtain similar behavioral output (i.e. probability of arousal). In parallel with electrical recordings, we also obtained video recordings. For tracking movement, either a red LED or a marker reflecting infrared light was placed on the head of the mice. Recorded video files (30 fps; MOTIVE Tracker camera system) were then analyzed with BONSAI53.

All data processing was carried out using MATLAB. EEG signals were down-sampled at 2 kHz and low-pass filtered for 50 Hz for further analysis. Power of delta (1-3 Hz), theta (5-8 Hz) and sigma (10-15 Hz) frequency bands were calculated from one of the frontal screw electrodes.

Electromyogram (EMG) signal was detected either directly from the neck muscle or indirectly from one of the parietal EEG screw electrode. For further analysis, EMG signal was down-sampled at 2 kHz and bandpass filtered between 300-600 Hz.

Comparison of EMG signal from the neck muscle or from EEG screw electrode gave similar results overall. However, the latter gave better signal-to-noise ratio and occasionally presented activity which couldn't be detected from neck muscle, possibly due to activity arise from the jaw and face muscles.

Sleep-wake states were determined using EEG and EMG signal. Wake was characterized by high muscle activity, and low delta power, while sleep was characterized by low muscle tone and was further subdivided into NREM and REM. NREM and REM were associated with high and low delta power, respectively. For the purpose of this study arousal refers to a change from either sleep states to the wake state. Theta power per se did not predict sleep stages. REM was determined as high theta/delta ratio associated with low delta power, but always confirmed by eye, creating a wavelet spectrogram from frontal and/or parietal EEG signal.

We considered arousal when motionless (e.g. stationary body posture), low EMG states was interrupted or followed by body motion or posture changes. These events were always accompanied by marked increase in EMG activity. Therefore to quantify the onset and duration of arousal, we used the EMG signal. First, all the recorded EMG time series were divided to 0.1 sec bins and standard deviation (SD) was calculated for each bin. Plotting a probability distribution for SD values of muscle activity, for each animal, we were able to determine a value (peak of the distribution) characteristic for muscle activity in sleep. Then, using a threshold – determined for each animal (+2.1-5 SD of baseline) – each time bin was assigned either EMG ON or EMG OFF. Two simple algorithms were applied to reduce fragmentation of EMG ON/OFF states. To reduce the detection of simple muscle twitches, and favor to those with real head movements, EMG ON states longer than 0.5 sec were kept, and those with shorter duration was regarded as EMG OFF. In order to reduce fragmentation of active states, EMG OFF states shorter than 2 sec were converted to EMG ON states if they were embedded into EMG ON (Supplementary Fig. 5).

Stimulus induced arousals (probability, onset, duration) were evaluated within a 60 sec long time window (if not stated otherwise), following stimulus onset. First, all trials were excluded (i) with EMG ON state within 10 sec preceding the stimulation, (~15 % of trials) (ii) with transient, e.g., no stable REM or NREM stages within 10 sec preceding the stimulation (<1% of trials). Spontaneous arousals were evaluated by exactly the same criteria, but for non-stimulated periods (beginning of a 60 sec time window, at 61-101 sec before stimulus onset). The vast majority of microarousals occurred within 10 sec after stimulus onset (Supplementary Fig. 5b), thus, any arousal bout with longer latency was not

considered here as evoked activity. Those, with no evoked EMG activity during the 60 sec periods, were assigned as sleep-through cases. Total stimulated trials containing all kind of stimulus durations and intensities involved in the analysis after exclusion (see above): 262 trials for 3 eYFP mice; 3173 trials for 8 ChR2-DMT mice and 3168 trials for 4 VB mice.

For microarousal experiments, 0.5, 1 and 2 sec long stimulations were applied regularly in every 3-5 minutes, for 4-6 hours a day. Stimulations having different laser intensities and durations were applied randomly. Long, 10 sec long stimulations were usually delivered at the beginning or end of the day only once. When animals awakened for longer periods, stimulation protocol was paused.

For Figs. 3f-l and 4a-f, we used high laser intensities (13-46 mW for 7 DMT animal) to achieve the possible highest arousal probability, and we used lower (0.001-4.3 mW for 1 DMT stimulation, and for 7 VB stimulation), when evoked microarousal probability was higher than 90 %.

When subthreshold effect was tested (Fig. 3m-q) during 1 sec stimulation, we analyzed trials with laser intensities generated comparable probabilities of microarousals in NREM sleep for each mice (35-66 % probability, inferred from intensity-probability curves presented on Supplementary Fig. 8). To calculate the recovery time constant for delta and sigma power, average curve for delta and sigma power for each animal were calculated in a 60 sec window and a single exponential was fitted on the recovery phase. In order to ensure reliable data acquisition laser power was continuously monitored and recorded.

We expressed state dependency as the ratio of maximal arousal probability evoked during REM and NREM sleep, corrected for baseline arousal rate (REMmax – REMspont)/ (NREMmax-NREMspont).

To investigate whether the prestimulus EEG delta and sigma powers determine the behavioral outcome of the stimulus (e.g. MA or ST, see Supplementary Fig. 7) continuous delta and sigma powers were divided into four sec bins and average power was calculated for each bin for both frequency bands. Mean values in each bin were normalized for the average values for each animals, than averaged across animals.

Single-unit freely moving recordings

Four custom fabricated tungsten tetrodes (d: 12.5 μm, California Fine Wire) were chronically implanted into the DMT of CR-Cre (AP -0.9, ML 0.6, DV 3.1-3.2 mm, at 10 degrees; n=4) mice along with multimode optic fiber (105 μm core diameter, NA = 0.22; Thorlabs), all tunneled in a polyimide tube (0.008 ID, Neuralynx). The tetrode wires were attached to an electrode interface board (EIB-16, Neuralynx) using gold electrode contact pins (Neuralynx). The EMG electrode wire as well as the ground and reference wires was soldered to the EIB. Before implantation, tetrodes were cut to final length (200-400 μm left between the optic fiber and tetrode tips); impedances measured at 1 kHz were kept between 300-700 kΩ. Ground and reference screws were implanted in the occipital and parietal bones, accordingly; an EMG wire was inserted into the neck muscle. Finally, all pieces were

secured onto the skull by multiple layers of dental acrylic (Paladur, Heraeus Kulzer). Mice were left at least 7 days to recover and then, handled for several days.

During recordings, animals were left in their homecage to sleep during their light phase (9 am- 7 pm). Behavior of mice was also video recorded (30 fps). The interface board was connected to an Intan recording system through a 16-channel preamplifier (Intan Technologies; gain: 192x, sampling frequency: 20 kS/sec). The laser was triggered via a data acquisition board (National Instruments) controlled by custom-built MATLAB programs. Analog trigger pulses were registered in parallel with the neural data. Short latency (10ms) light-evoked spiking was considered reliable to indicate direct light activation, thus, enabled the identification of the DMT/CR+ cell type.

EMG onset as an indicator for sleep/wake transition was given as described above. Awake periods were only accepted in case when they were preceded by a 30 sec sleeping phase and were longer than 500 ms, defined as the lower limit for minimal arousal.

Noise filtering was made on the raw electrophysiological recordings by average subtraction, and then, it was filtered for spikes (>400 Hz). Spike detection and principal component analysis-based automatic clustering were performed using SpikeDetekt and KlustaKwik, respectively. Cell-grouping was refined manually by KlustaKwik54. A group of spikes were considered to be generated by a single neuron if the waveforms formed a discrete, well-isolated cluster and had an autocorrelogram with absolute refractory period. We excluded the cells from different tetrodes which shared a symmetric crosscorrelogram as well as a similar action potential shape in order to avoid enumerating the same cell more than one time.

Optogenetic identification of DMT/CR+ single units was done with 5 ms long, low intensity, 473 nm laser pulses (100-500 μW) at 1 Hz to evoke spiking. The lower laser intensities explain the difference in response latencies and probability between the anesthetized and the freely moving preparations. Higher laser intensities obstructed the unequivocal clustering of single units in freely moving conditions.

DMT/CR+ neurons were chosen upon a criterion of a tagging z-score above 3.3 ($p > 0.001$) in the first 10 ms after light onset. Every cell showing weaker or no photoactivation was considered to be non-CR+ cells. However, as large proportion of the DMT cells is CR+, and the viral infection rate is very high (Supplementary Figure 1), it cannot be ruled out that DMT/CR+ cells were occasionally considered to be DMT/CR-negative due to e.g. their weaker activation. Indeed, the similarity in activity preceding EMG ON states between DMT/CR+ and some CR- cells suggests that this could happen frequently. Peri-event time histograms (PSTH) were defined for each cell around the detected EMG onsets. Z-score values of the firing rates were given upon PSTH calculation for each cell to a 20 sec baseline (sleep) period (between -30 sec and -10 sec calculated from the onset of EMG signal). Significant changes of the firing rates were defined upon at least two significant ($z > 1.64$, $p > 0.05$) neighbor z-score (1 s) bins in the [-10 10] sec interval around EMG onset. Mean z-score for CR+ and CR- neurons is presented. All data analysis was carried out using custom-built MATLAB software.

Open field behavior

The apparatus consists of a Plexiglas open field (40 cm × 40 cm × 40 cm). DMT of male CR-Cre mice (3–6 months old) were injected with either AAV2/5-Ef1a-DIO-SwichRCA-eYFP or AAV2/5-Ef1a-DIO-eYFP (for controls) and an optic fiber was implanted above the DMT. After 4 weeks of recovery, mice were placed into the open field chamber for 10 mins. The first minute served as habituation phase, then, it was followed by 3 x 3 mins of testing periods (OFF-ON-OFF). Based on the juxtacellular recordings (Supplementary Figure 4) we applied, 2 sec of continuous laser light illuminations (10 mW) at every 30 sec during the ON period to inactivate the DMT/CR+ population. The number of brief behavioral immobile periods (stops) was quantified as a sign of lowered arousal periods. Stops longer than 2 sec (<1.7% of total time) were discarded. Effects of within groups and between groups were analyzed with Repeated-measures ANOVA.

Retrograde tracing

Single retrograde tracings were carried out with Cholera Toxin B subunit (CTB; List Biological Laboratories: 104), while double retrograde tracings with CTB and Fluorogold (FG; Fluorocrome). Both tracers were iontophoretically injected (7-7 sec on/off duty cycle; 2-3 μA, for 10 min) into one of the following brain areas: NAc (n = 13), PrL (n = 15) or BLA (n = 15) under ketamine (75 mg/kg) / xylazine (5 mg/kg) anesthesia. After one week of survival time, the animals were perfused; then, brains were cut into 50 μm thick coronal sections. Free-floating sections were intensively washed with PB and then, treated with a blocking solution containing 10 % NDS and 0.5 % Triton-X for 30 minutes at room temperature. The primary antibodies against CTB (goat; List Biological Laboratories: 703; 1:20000), FG (rabbit; Chemicon: AB153; 1:10000), PV (mouse; Swant: PV 234; 1:3000) and CR (mouse; Swant; 1:3000) were diluted in PB containing 0.1 % NDS and 0.1 % Triton-X. After primary antibody incubation (1 day at room temperature or 2-3 days, at 4 °C), sections were treated with Alexa 488-conjugated donkey anti-rabbit IgG, Cy3-conjugated donkey anti-goat and A647/CY5-conjugated donkey anti-mouse (respectively) for 2 hrs at room temperature.

cFos experiments

Neuronal activation to distinct external stimuli was monitored via cFos expression. In wake-sleep cycle experiment, animals were perfused according to the Zeitgeber Time (ZT): at 2.5h in sleeping (light) phase and 14.5 in awake (dark) phase (n = 8, each). In experiments measuring the effect of increasing arousal, control animals (n = 4) were handled for two days animals, the habituation group (n = 4) were placed in the shock chamber for 5 min without receiving foot-shock after two days of handling, while shocked animals (n = 4) received 2 sec 1 mA foot-shock every 30 sec for 4 mins in the same chamber. After 60 mins, animals were perfused. CFos and CR double stainings were performed on 50 μm thick coronal sections containing DMT. The primary antibodies against cFos (rabbit; Calbiochem: Ab-5; 1:20000) and calretinin (CR; mouse; Swant; 1:3000) were diluted in PB containing 0.1 % NDS and 0.1 % Triton-X. 24-48h later, sections were treated with Alexa 488-conjugated and Cy3-conjugated secondary antibodies for 2h at room temperature. After

further PB washes, sections were mounted in Vectashield and imaged using confocal microscope.

For quantification of cFos density, the anti-cFos antibody was developed with DABNi as a chromogen. The section was dehydrated and then, mounted with DePex (Serva, Heidelberg, Germany). All sections used for quantification were developed together for the same duration. Images were taken using bright-field, epifluorescent (Zeiss) or confocal microscope (Zeiss, Olympus and Nikon). 3 sections were analyzed per animals: one-one from the rostral, middle and caudal part of the DMT separated by 600 μm. The CR-content of single retrogradely, the CTB+FG double retrogradely labeled and cFos activated cells were analyzed manually on 60x confocal images. The number of cFos-labeled cells was analyzed using a custom-written ImageJ script.

Single-cell labeling and reconstruction

Single DMT neurons were transfected with RNA construct that drives the expression of the green fluorescent protein eGFP associated with the palmytolation signal GAP43, that specifically direct it to the axonal membrane55. Transfections were carried out following a recently described method of "in vivo" RNA electroporation in a high saline vehicle56. Briefly, borosilicate micropipettes (20 um tip) were backfilled with a RNA solution (1.8 μg/μl) in a high saline vehicle (NaCl 0.5M) and mounted on a holder implemented with a pressure pump connection and an electrode. The micropipette was positioned into the DMT, and 50-100 nl of the RNA solution were slowly injected using a precision electro-valve system (Picospritzer II, Parker Hannifin, Cleveland OH). Two to four 200 Hz trains of 1ms negative square pulses at 50V were then applied using a CS20 stimulator (Cibertec, Madrid, Spain). After 52-65 hrs survival, the animals were perfused and serial 50-μm-thick coronal sections were obtained. First, the GFP signal was intensified with anti-GFP (rabbit, Millipore, 1:10000) staining, then, counterstained for CR. Finally, all the sections were immunostained, free-floating, in anti-GFP serum followed by incubation with a biotinylated goat anti-rabbit serum (1:300; Sigma–Aldrich, St. Louis, MO, USA) and an avidin-biotin-peroxidase kit (1:300; Vectastain Elite, Vector Laboratories, Burlingame, CA, USA). Sections were serially mounted, dehydrated and cover slipped with DePeX. Axonal arbor of one cell was reconstructed using a Camera Lucida tube.

Parallel immunostainings of the human and mice thalamus

Postmortem human brains were removed 2–5 h after death. The internal carotid and the vertebral arteries were cannulated, and the brains were perfused first with physiological saline (1.5 l in 30 min) containing heparin (5 ml), followed by a fixative solution containing 4% paraformaldehyde, 0.05% glutaraldehyde and 0.2% picric acid (vol/vol) in 0.1 M PB, pH = 7.4 (4–5 l in 1.5–2 h). The thalamus was removed from the brains after perfusion, and was postfixed overnight in the same fixative solution, except for glutaraldehyde, which was excluded. Mouse brains obtained via perfusion. Subsequently, 50-μm thick coronal sections were obtained for immunohistochemistry using a Leica VTS-1000 Vibratome (Leica Microsystems). The sections were incubated against CR, vGluT2 (mouse, Millipore: MAB5504, 1:3000) and Orx-staining. The signals were visualized with either the DAB or DAB-Ni reaction. Afterwards, in some cases, glucose (7%, wt/vol) was added to the OsO4

solution to preserve the color difference. The sections were dehydrated and cover slipped with DePeX.

Estimation of the length of thalamic axons in the prelimbic cortex using a retro-anterograde viral labeling

We utilized the fact that in the CR-Cre mice, the Cre-dependent-AAV vectors used here propagated both in anterograde and retrograde manner after sufficiently long survival time (>6 weeks). Thus, virus injection into target A of DMT/CR+ cells back-labeled CR+ neurons in a retrograde manner. If the neurons projecting to target A had collaterals in target B, the virus propagated in an anterograde fashion and visualized axons in target B as well. Obviously, to demonstrate that these axons in target B belongs to the DMT cells and not to other calretinin neurons we should demonstrate that (i) target A contains no calretinin cells which project to target B, (ii) there are no other region outside DMT which project to both target A and B. For this analysis we selected the three main targets PrL, NAc and AMY. Injection of the AAV virus into any of these targets (n= 8, 9, 12 cases, for PrL, NAc, AMY, respectively) labeled abundant cell populations in the DMT but no cell bodies could be found in the other two regions, demonstrating the lack of CR+ projecting cells among these three centers. The virus injection, however, did label scattered neurons in the dorsal/caudal hypothalamus and the VTA following PrL and NAc injections indicating a minor calretinin-positive projection arising outside the thalamus. Using sections from the double retrograde CTB+FG experiments described above, however, we found only a small fraction of CR+ cells (< 2%), which projected to any two of these three targets (Supplementary Figure. 11). Based on these data, we can firmly conclude that following virus injection to PrL, NAc, or AMY, the axons labeled in any other two regions are collaterals of branching DMT/CR+ axons. The experiments indeed demonstrated that injection to any of these three targets labeled abundant axon arbors in the other two.

Then, cortical projections of all DMT cells as well as NAc and Amy-projecting DMT cells were analyzed in frontal cortical sections as follows. The native fluorescent signal was analyzed in 50 μm coronal sections. PrL cortex was divided into 50 μm thick bins from the pia to the bottom of L6 that were positioned perpendicular with the pia surface. In each bin, the image stacks were thresholded to optimally select the axonal branches containing tracer. The thresholded image was reduced to skeletons using the following FIJI plugin Plugins/ Skeleton/Skeltonize (2D/3D). Then measured by another plugin Analyze/Skeleton/Analyze Skeleton (2D/3D). This measures the length of the segments of the skeletonized structures. The lengths were summarized for a given area, then, the values were normalized to 10 000 μm^3. Six sampling areas were investigated in each animal (n=9); the results from the same animal were averaged and displayed as mean ± SD.

The distribution of the vGluT2 terminals were mapped by optical fractionators method[57]: the number of vGluT2+ terminals were counted in 50x50 μm counting frames placed on grid points of a 500x500 μm sampling grid for human samples and 10x10 μm counting frames placed on grid point of a 50x50 μm sampling grid for mouse samples in the upper 5 μm of the section. The density of boutons were normalized to 1/1000 μm^2. The grid data were interpolated with MATLAB (MathWorks) and displayed as a heat map. The distribution of

CR+ cells were mapped with Neurolucida (MBF Biosciences) and displayed as dot plot (Fig. 7) on the top of the vGluT2 heat maps.

Statistical analysis

No statistical methods were used to predetermine sample size but our sample sizes are similar to those reported in previous publications[58],[59]. Experiments and/or analysis described in Figs 1a-e, 2 a-e, 3i-k, o-q, 4d-i, 5k-q, 6a-g and Supplementary Figs 1e-i, 5 b,c, 6-8, 9l-n, 10c,d, 11a-l and 12p-r were randomized; all other experiments were not. In all experiments investigators were blinded to allocation and outcome assessments except in the cases of tracer/viral tracing. Data in Figures represent mean ± SEM unless otherwise indicated. Data from independent experiments were pooled when possible. Sample sizes were chosen based upon pilot experiments in order to accurately detect statistical significance as well as considering technical feasibility and ethical animal and sample use. Statistical significance was assessed using two-tailed t-test, Mann–Whitney U test or ANOVA after testing normality of the dataset, using Kolmogorov-Smirnov test. Statistical analyses were performed using STATISTICA (Statsoft) or SPSS 15. Significance is labeled as: *p < 0.05, **p < 0.01, ***p < 0.001; n.s., not significant.

Supplementary Material

Refer to Web version on PubMed Central for supplementary material.

Acknowledgements

Reporting Summary. Further information on experimental design is available in the Nature Research Reporting Summary linked to this article.

Data and code availability. The data and code that support the findings of this study are available from the corresponding author upon reasonable request.

Author contributions

Competing interests

The authors declare no competing financial interests.

References

1. Saper CB, Fuller PM, Pedersen NP, Lu J, Scammell TE. Sleep state switching. Neuron. 2010; 68:1023–42. [PubMed: 21172606]

2. Brown RE, Basheer R, McKenna JT, Strecker RE, McCarley RW. Control of sleep and wakefulness. Physiol Rev. 2012; 92:1087–187. [PubMed: 22811426]

3. Halász, P, Bódizs, R. Dynamic Structure of NREM Sleep. Springer-Verlag; 2013.

4. Terzano MG, Parrino L. Origin and Significance of the Cyclic Alternating Pattern (CAP). REVIEW ARTICLE. Sleep Med Rev. 2000; 4:101–123. [PubMed: 12531162]

5. Schieber JP, Muzet A, F P. Phases of spontaneous transitory activation during normal sleep in humans. Arch Sci Physiol. 1971; 25:443–65.

6. Sakurai T. The neural circuit of orexin (hypocretin): Maintaining sleep and wakefulness. Nat Rev Neurosci. 2007; 8:171–81. [PubMed: 17299454]

7. Van der Werf YD, Witter MP, Groenewegen HJ. The intralaminar and midline nuclei of the thalamus. Anatomical and functional evidence for participation in processes of arousal and awareness. Brain Res Brain Res Rev. 2002; 39:107–40. [PubMed: 12423763]

8. Kirouac GJ. Placing the paraventricular nucleus of the thalamus within the brain circuits that control behavior. Neurosci Biobehav Rev. 2015; 56:315–29. [PubMed: 26255593]

9. Colavito V, Tesoriero C, Wirtu AT, Grassi-Zucconi G, Bentivoglio M. Limbic thalamus and state-dependent behavior: the paraventricular nucleus of the thalamic midline as a node in circadian timing and sleep/wake-regulatory networks. Neurosci Biobehav Rev. 2015 Jul.:3–17. [PubMed: 25479103]

10. Unzai T, Kuramoto E, Kaneko T, Fujiyama F. Quantitative Analyses of the Projection of Individual Neurons from the Midline Thalamic Nuclei to the Striosome and Matrix Compartments of the Rat Striatum. Cereb Cortex. 2017; 27:1164–1181. [PubMed: 26672610]

11. Lövblad KO, Bassetti C, Mathis J, Schroth G. MRI of paramedian thalamic stroke with sleep disturbance. Neuroradiology. 1997; 39:693–8. [PubMed: 9351103]

12. Hermann DM, et al. Evolution of Neurological, Neuropsychological and Sleep-Wake Disturbances After Paramedian Thalamic Stroke. Stroke. 2008; 39:62–68. [PubMed: 18048862]

13. Jones EG. The thalamic matrix and thalamocortical synchrony. Trends Neurosci. 2001; 24:595–601. [PubMed: 11576674]

14. Fuller PM, et al. Reassessment of the structural basis of the ascending arousal system. J Comp Neurol. 2011; 519:933–56. [PubMed: 21280045]

15. Anaclet C, et al. Basal forebrain control of wakefulness and cortical rhythms. Nat Commun. 2015; 6:8744. [PubMed: 26524973]

16. Winsky L, Montpied P, Arai R, Martin BM, Jacobowitz DM. Calretinin distribution in the thalamus of the rat: immunohistochemical and in situ hybridization histochemical analyses. Neuroscience. 1992; 50:181–196. [PubMed: 1407555]

17. Fortin M, Asselin MC, Gould PV, Parent A. Calretinin-immunoreactive neurons in the human thalamus. Neuroscience. 1998; 84:537–548. [PubMed: 9539224]

18. Peng ZC, Grassi-Zucconi G, Bentivoglio M. Fos-related protein expression in the midline paraventricular nucleus of the rat thalamus: basal oscillation and relationship with limbic efferents. Exp brain Res. 1995; 104:21–9. [PubMed: 7621938]

19. Otake K, Kin K, Nakamura Y. Fos expression in afferents to the rat midline thalamus following immobilization stress. Neurosci Res. 2002; 43:269–282. [PubMed: 12103445]

20. Zhu L, Wu L, Yu B, Liu X. The participation of a neurocircuit from the paraventricular thalamus to amygdala in the depressive like behavior. Neurosci Lett. 2011; 488:81–86. [PubMed: 21073922]

21. Bubser M, Scruggs JL, Young CD, Deutch AY. The distribution and origin of the calretinin-containing innervation of the nucleus accumbens of the rat. Eur J Neurosci. 2000; 12:1591–1598. [PubMed: 10792437]

22. Do-Monte FH, Quiñones-Laracuente K, Quirk GJ. A temporal shift in the circuits mediating retrieval of fear memory. Nature. 2015; 519:460–3. [PubMed: 25600268]

23. Penzo MA, et al. The paraventricular thalamus controls a central amygdala fear circuit. Nature. 2015; 519:455–9. [PubMed: 25600269]

24. Steriade M, Oakson G, Ropert N. Firing rates and patterns of midbrain reticular neurons during steady and transitional states of the sleep-waking cycle. Exp Brain Res. 1982; 46:37–51. [PubMed: 7067790]

25. Beas BS, et al. The locus coeruleus drives disinhibition in the midline thalamus via a dopaminergic mechanism. Nature Neuroscience. 2018; doi: 10.1038/s41593-018-0167-4

26. Berndt A, Lee SY, Ramakrishnan C, Deisseroth K. Structure-guided transformation of channelrhodopsin into a light-activated chloride channel. Science. 2014; 344:420–4. [PubMed: 24763591]

27. Watson BO, Levenstein D, Greene JP, Gelinas JN, Buzsáki G. Network Homeostasis and State Dynamics of Neocortical Sleep. Neuron. 2016; 90:839–52. [PubMed: 27133462]

28. Lecci S, Fernandez LM, Weber FD, Cardis R, Chatton J, Born J, L A. Coordinated infraslow neural and cardiac oscillations mark fragility and offline periods in mammalian sleep. Sci Adv. 2017; 3:e1602026. [PubMed: 28246641]

29. Otake K, Nakamura Y. Single midline thalamic neurons projecting to both the ventral striatum and the prefrontal cortex in the rat. Neuroscience. 1998; 86:635–649. [PubMed: 9881876]

30. Dong X, Li S, Kirouac GJ. Collateralization of projections from the paraventricular nucleus of the thalamus to the nucleus accumbens, bed nucleus of the stria terminalis, and central nucleus of the amygdala. Brain Structure and Function. 2017; :1–17. DOI: 10.1007/s00429-017-1445-8

31. Pare D, Smith Y. Thalamic collaterals of corticostriatal axons: their termination field and synaptic targets in cats. J Comp Neurol. 1996; 372:551–67. [PubMed: 8876453]

32. Zhang L, Kolaj M, Renaud LP. Suprachiasmatic nucleus communicates with anterior thalamic paraventricular nucleus neurons via rapid glutamatergic and gabaergic neurotransmission: state-dependent response patterns observed in vitro. Neuroscience. 2006; 141:2059–66. [PubMed: 16797851]

33. Pedersen NP, et al. Supramammillary glutamate neurons are a key node of the arousal system. Nat Commun. 2017; 8:1405. [PubMed: 29123082]

34. Fremeau RT Jr, et al. The expression of vesicular glutamate transporters defines two classes of excitatory synapse. Neuron. 2001; 31:247–60. [PubMed: 11502256]

35. Fortin M, Asselin MC, Gould PV, Parent A. Calretinin-immunoreactive neurons in the human thalamus. Neuroscience. 1998; 84:537–548. [PubMed: 9539224]

36. Cicchetti F, Lacroix S, Beach TG, Parent A. Calretinin gene expression in the human thalamus. Mol Brain Res. 1998; 54:1–12. [PubMed: 9526028]

37. Gent TC, Bandarabadi M, Herrera CG, Adamantidis AR. Thalamic dual control of sleep and wakefulness. Nat Neurosci. 2018; 21:974–984. [PubMed: 29892048]

38. Matyas F, et al. Motor control by sensory cortex. Science. 2010; 330:1240–3. [PubMed: 21109671]

39. Hunter J, Jasper HH. Effects of thalamic stimulation in unanaesthetised animals; the arrest reaction and petit mal-like seizures, activation patterns and generalized convulsions. Electroencephalogr Clin Neurophysiol. 1949; 1:305–24. [PubMed: 18135423]

40. Moruzzi G, Magoun HW. Brain stem reticular formation and activation of the EEG. Electroencephalogr Clin Neurophysiol. 1949; 1:455–73. [PubMed: 18421835]

41. Schlag JD, Chaillet F, Herzet JP. Thalamic reticular system and cortical arousal. Science. 1961; 134:1691–2. [PubMed: 14498495]

42. Vanderwolf CH, Stewart DJ. Thalamic control of neocortical activation: a critical re-evaluation. Brain Res Bull. 1988; 20:529–38. [PubMed: 3395864]

43. Padilla-Coreano N, Do-Monte FH, Quirk GJ. A time-dependent role of midline thalamic nuclei in the retrieval of fear memory. Neuropharmacology. 2012; 62:457–463. [PubMed: 21903111]

44. Zhu Y, Wienecke CFR, Nachtrab G, Chen X. A thalamic input to the nucleus accumbens mediates opiate dependence. Nature. 2016; 530:219–222. [PubMed: 26840481]

45. Choi EA, McNally GP. Paraventricular Thalamus Balances Danger and Reward. J Neurosci. 2017; 37:3018–3029. [PubMed: 28193686]

46. Do-Monte FH, Minier-Toribio A, Quiñones-Laracuente K, Medina-Colón EM, Quirk GJ. Thalamic Regulation of Sucrose Seeking during Unexpected Reward Omission. Neuron. 2017; 94:388–400.e4. [PubMed: 28426970]

47. Betley JN, et al. Neurons for hunger and thirst transmit a negative-valence teaching signal. Nature. 2015; 521:180–185. [PubMed: 25915020]

48. Labouèbe G, Boutrel B, Tarussio D, Thorens B. Glucose-responsive neurons of the paraventricular thalamus control sucrose-seeking behavior. Nat Neurosci. 2016; 19:999–1002. [PubMed: 27322418]

49. Christoffel DJ, et al. Excitatory transmission at thalamo-striatal synapses mediates susceptibility to social stress. Nat Neurosci. 2015; 18:962–4. [PubMed: 26030846]

50. Yerkes RM, Dodson JD. The relation of strength of stimulus to rapidity of habit-formation. J Comp Neurol Psychol. 1908; 18:459–482.

51. Umbriaco D, Watkins KC, Descarries L, Cozzari C, Hartman BK. Ultrastructural and morphometric features of the acetylcholine innervation in adult rat parietal cortex: An electron microscopic study in serial sections. J Comp Neurol. 1994; 348:351–373. [PubMed: 7844253]

52. Pinault D. A novel single-cell staining procedure performed in vivo under electrophysiological control: Morpho-functional features of juxtacellularly labeled thalamic cells and other central neurons with biocytin or Neurobiotin. J Neurosci Methods. 1996; doi: 10.1016/0165-0270(95)00144-1

53. Lopes G, et al. Bonsai: an event-based framework for processing and controlling data streams. Front Neuroinform. 2015; 9:7. [PubMed: 25904861]

54. Rossant C, et al. Spike sorting for large, dense electrode arrays. Nat Neurosci. 2016; 19:634–641. [PubMed: 26974951]

55. Furuta T, et al. In vivo transduction of central neurons using recombinant Sindbis virus: Golgi-like labeling of dendrites and axons with membrane-targeted fluorescent proteins. J Histochem Cytochem. 2001; 49:1497–1508. [PubMed: 11724897]

56. Porrero C, et al. A Simple and Efficient In Vivo Non-viral RNA Transfection Method for Labeling the Whole Axonal Tree of Individual Adult Long-Range Projection Neurons. Front Neuroanat. 2016; 10

57. Harsan L-A, et al. Mapping remodeling of thalamocortical projections in the living reeler mouse brain by diffusion tractography. Proc Natl Acad Sci. 2013; 110:E1797–E1806. [PubMed: 23610438]

58. Giber K, et al. A subcortical inhibitory signal for behavioral arrest in the thalamus. Nat Neurosci. 2015; 18:562–568. [PubMed: 25706472]

59. Barthó P, et al. Ongoing Network State Controls the Length of Sleep Spindles via Inhibitory Activity. Neuron. 2014; 82:1367–1379. [PubMed: 24945776]
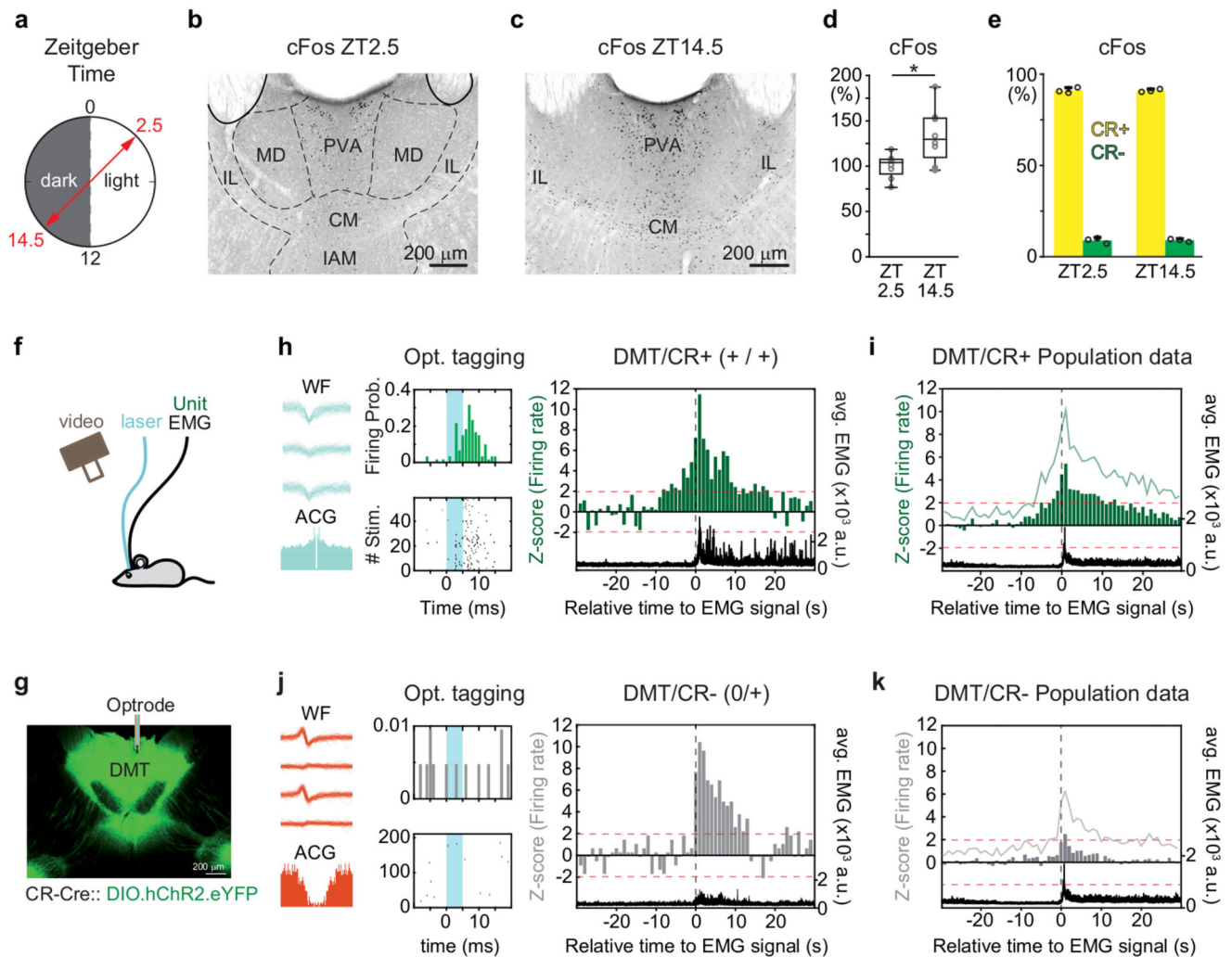
Figure 1. DMT/CR+ cells show arousal-related activation

a, Experimental setting for cFos immunostaining in DMT at two distinct time points of the dark-light phase according to the Zeitgeber Time (ZT).

b-c, Representative images of cFos expression in DMT at ZT2.5 (dark phase) and at ZT14.5 (light phase).

d, Quantitative data for cFos expression at ZT14.5 normalized to ZT2.5 in DMT (n = 8-8 mice; two-tailed unpaired *t*-test, t(14) = -2,826, p = 0,0135).

e, Co-localization of CR in cells displaying cFos positivity at ZT2.5 (light phase, n=3 mice, 1140/1253 neurons) and ZT14.5 (dark phase, n=3 mice, 1565/1723 neurons).

f, Schematic drawing for electrophysiological recordings of DMT cells during natural sleep.

g, Confocal image of a coronal section with cannula track (white bar) guiding optrode into the AAV-ChR2-eYFP (green) labeled DMT/CR+ region.

h, Waveforms (WF) in three out of the four tetrode electrodes, autocorrelogram (ACG; left, bottom) and peri-event time histogram upon optogenetic tagging of a DMT/CR+ cell (middle). *Right*, the same cell started to increase its firing activity preceding the behavioral

arousal (black dashed line) by several seconds and maintained elevated firing after the EMG onset as well. '+/+, increased activity before/after the arousal; black trace, EMG signal.

i, Population data for the activity of DMT/CR+ at the sleep/wake transition (n = 31 neurons).

j, As in **h**, for a non-tagged (putative CR-) cell. Note the lack of significant increase in firing activity before the onset of movement.

k, Population data for the activity of DMT/CR- units at the sleep/wake transition (n = 34 neurons). 1 sec bins indicates the averages of z-scores. Green lines, variance (SD) of z-scores; black, averaged EMG signal; black vertical dashed line, EMG onset; red horizontal dashed line, z-score value 1.96 ($p < 0.05$). Bar graphs are means ± SD; open circles in **d** and **e** represent data for single animals; the horizontal lines in the box plots indicate medians, the box limits indicate first and third quantiles, and the vertical whisker lines indicate minimum and maximum values. *$p < 0.05$. CM, central medial thalamic nucleus; IAM, interanteromedial thalamic nucleus; IL, intralaminar thalamic nuclei; MD, mediodorsal thalamic nuclei; PVA, paraventricular thalamic nucleus, anterior part.
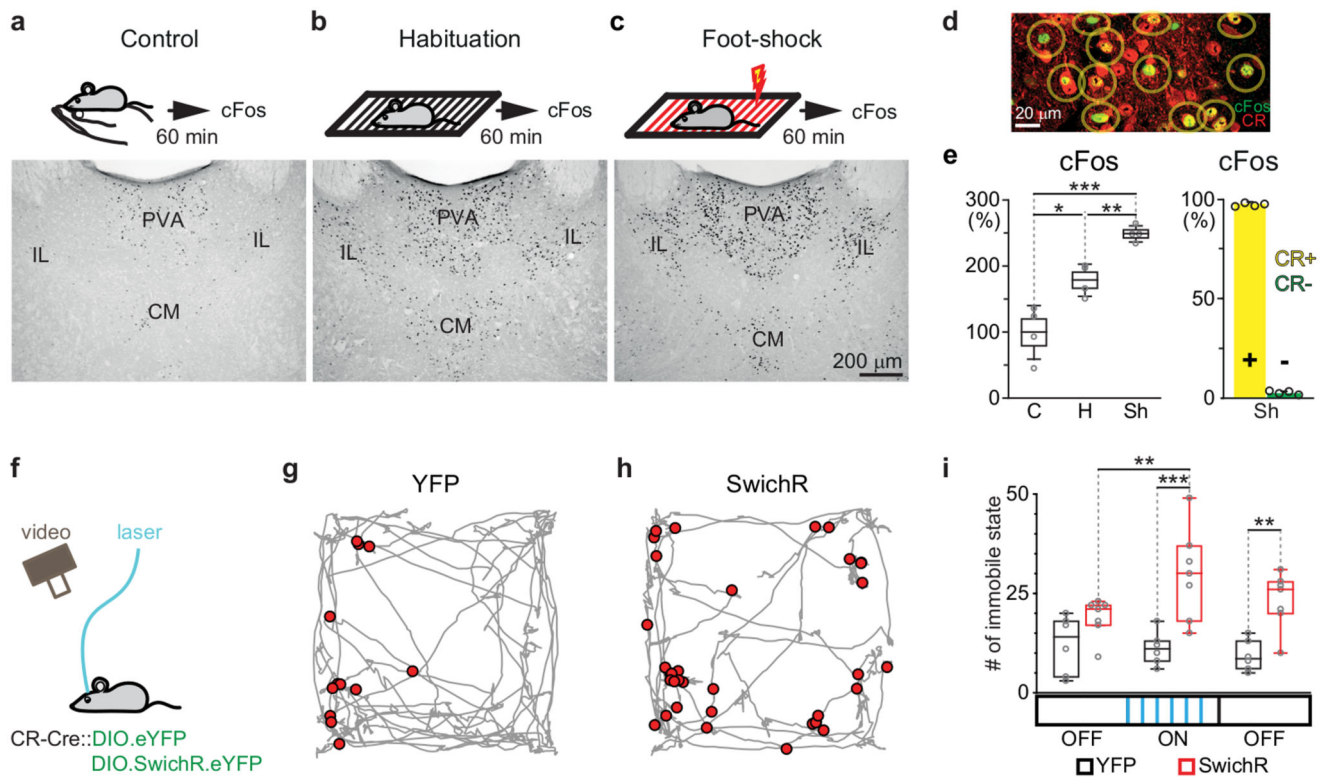
Figure 2. cFos content and optogenetic inhibition of DMT/CR+ cells in situations with distinct arousal levels

a-c, Schematic drawing of the experimental design (top) and representative images of cFos expressions (bottom) in DMT following handling (**a**), habituation (no shock); **b**) and foot shock (**c**).

d, Representative confocal image of the co-localization of cFos and CR in DMT cells in a foot-shock case.

e, Left, Normalized data for cFos expressing DMT cells in Control (C), Habituation (H) and Shock (Sh) situations (n= 4-4mice; control: 100 ± 40%; habituation: 179 ± 24%, shock: 249 ± 12%; two-tailed unpaired t-test, C vs. H, t(6) = -3,339, p = 0.0156; H vs. Sh, t(6) = -5,152, p = 0.0021; C vs. Sh, t(6) = -7,043, p = 0.0004). Right, CR-content (right) of cFos expressing cells in case of Sh. Yellow bar indicates CR+/cFos+ cells (1393/1433 neurons, 97.2%; n=4 mice), green bar CR-/cFos+ cells (40/1433, neurons, 2.8%).

f, Schematic drawing for optogenetic inhibition of DMT/CR+ in a novel environment.

g-h, Representative data for short immobile states (red dots) evoked by optogenetic silencing during the exploration of a novel box (grey) in a YFP (control, **g**) and a SwichR-injected mouse (**h**).

i, Population data for the number of immobile states during the pre-OFF (3 mins), ON (3 mins) and post-OFF (3 mins; see Methods) periods in the YFP (n = 6 mice; pre OFF n = 12.2± 3.0; ON period n = 11.2 ± 1.7, post OFF n = 9.3 ± 1.6) and SwichR-injected animals (n = 7 mice; pre OFF n = 18.9 ± 1.9; ON period n = 29.9 ± 4.4, post OFF n = 23.3 ± 2.7). Repeated-measures ANOVA with Fisher's LSD, F(2, 22) = 3.4945, p = 0.0481. CM, centromedial thalamic nucleus; IL, intralaminar thalamic nuclei; PVA, paraventricular

thalamic nucleus, anterior part. Bar graphs are means ± SD**;** open circles in **e** and **i** represent data for single animals; the horizontal lines in the box plots indicate medians, the box limits indicate first and third quantiles, and the vertical whisker lines indicate minimum and maximum values. *p < 0.05; **p < 0.01, ***p < 0.001.
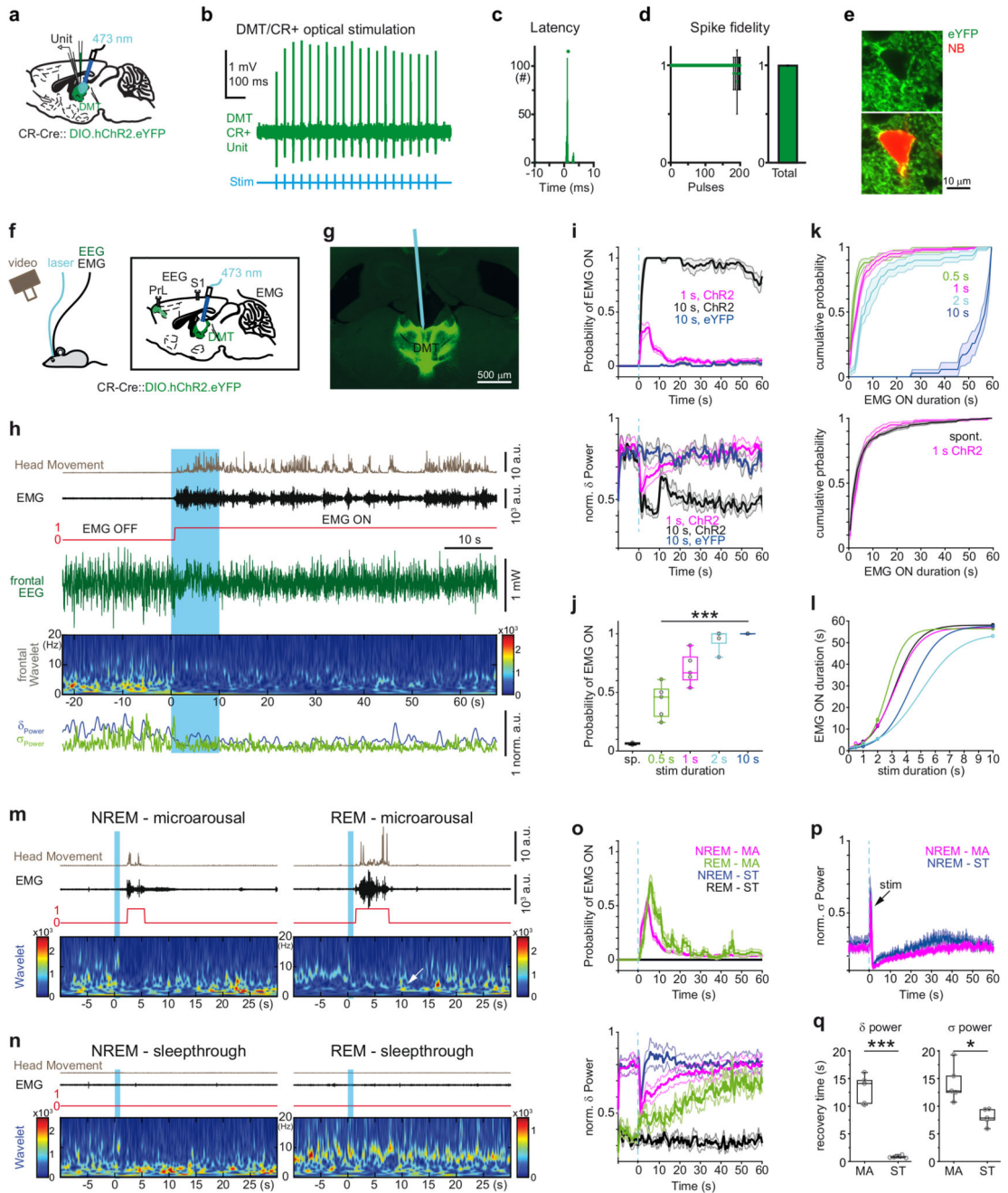
Figure 3. Stimulation of DMT/CR+ induces behaviorally relevant arousal patterns.

a, Experimental setting for anaesthetized in vivo recordings.

b, Optogenetic tagging of a DMT/CR+ cell.

c, Peri-event time histogram of light-evoked spike latency.

d, Spike response probability to 10 sec 20 Hz stimulation (left). Summated values (right).

e, Confocal fluorescent image of an optogenetically tagged, ChR2-eYFP-positive (green) and neurobiotin (red) filled DMT neuron.

f, Experimental setting for *in vivo* recordings and optogenetic stimulation in freely sleeping mice.

g, *Post hoc* identification of the optic fiber's track among ChR2-eYFP-expressing DMT/CR + neurons.

h, Persistent arousal evoked by 10 sec optogenetic stimulation of DMT/CR+ (blue period).

i, Average (mean) peri-event distribution of EMG ON states (top) and the corresponding delta power (bottom) in mice (n = 8) expressing ChR2 in DMT/CR+ cells after 1 and 10 sec stimulations (red and black, respectively). Data from control (YFP) mice are shown with blue (n = 3). Blue vertical dashed line, onset of the optogenetic stimulation.

j, Average probability of spontaneous and evoked arousal using different stimulus durations (n = 5 mice, spontaneous (sp), 0.06 ± 0.01; 0.5 sec, 0.43 ± 0.15; 1 sec, 0.70 ± 0.14; 2 sec, 0.95 ± 0.09; 10 sec, 1.00 ± 0; Repeated measures of ANOVA for evoked trials, $F(3,12) = 34.307$, $p < 0.0001$; pairwise comparison with Bonferroni correction shows significant difference only for 0.5 sec vs 1 sec, $p = 0.017$; 0.5 sec vs 2 sec, $p = 0.019$; 0.5 sec vs 10 sec, $p = 0.006$).

k, Cumulative probability distribution of the duration of EMG ON states in case of 0.5, 1, 2, and 10 sec stimulations (n = 5 mice) (top). Comparison of spontaneous and evoked microarousals (1 sec stimulation, bottom): 3.69 ± 1.31 sec for evoked and 3.23 ± 1.27 sec for spontaneous, n = 8 mice; two-tailed paired *t*-test for group data, $t(7) = -1.82$, $p = 0.111$; Kolmogorov-Smirnov test for animal-wise comparison, $p > 0.05$; in 7/8 animal).

l, Correlation of stimulus durations and arousal lengths in five individual animals fitted with sigmoid.

m, Microarousals during NREM (left) and REM (right) states evoked by 1 sec long stimulation of DMT/CR+ cells. Note the state change from REM to NREM after REM microarousals indicated by the appearance of high values in the delta range (white arrow).

n, Subthreshold stimulations (sleep-through) during NREM (left) and REM (right) states.

o, Average (mean) peri-event distribution of EMG ON states (top) and delta power (bottom) in case of microarousals (MA) and sleep-throughs (ST) during NREM and REM states (n = 5 mice). Note longer microarousals in REM (green, top), the return of NREM after REM MA indicated by the increasing delta values. Note also the rapid return of delta power in case of NREM-ST (bottom).

p, Prolonged disruption of sigma band both in case of microarousals MA and sleep-through. The sharp peak at time 0 (black arrow) represents the evoked response of 10 Hz stimulation in the frontal cortex.

q, Recovery time constants for delta and sigma powers in case of NREM microarousals and sleep-throughs (n = 5 mice, Delta-MA, 13.12 ± 2.34 sec; Delta-ST, 0.85 ± 0.23 sec; two-tailed paired *t*-test $t(4) = 11.116$, $p < 0.0001$ and Sigma-MA, 14.14 ± 2.98 sec; Sigma-ST, 8.03 ± 1.32 sec ; two-tailed paired *t*-test $t(4) = 4.114$, $p = 0.015$).

The horizontal lines in the box plots indicate medians, the box limits indicate first and third quantiles, and the vertical whisker lines indicate minimum and maximum values. *$p < 0.05$; ***$p < 0.001$. Shaded areas represent $\pm$ s.e.m.
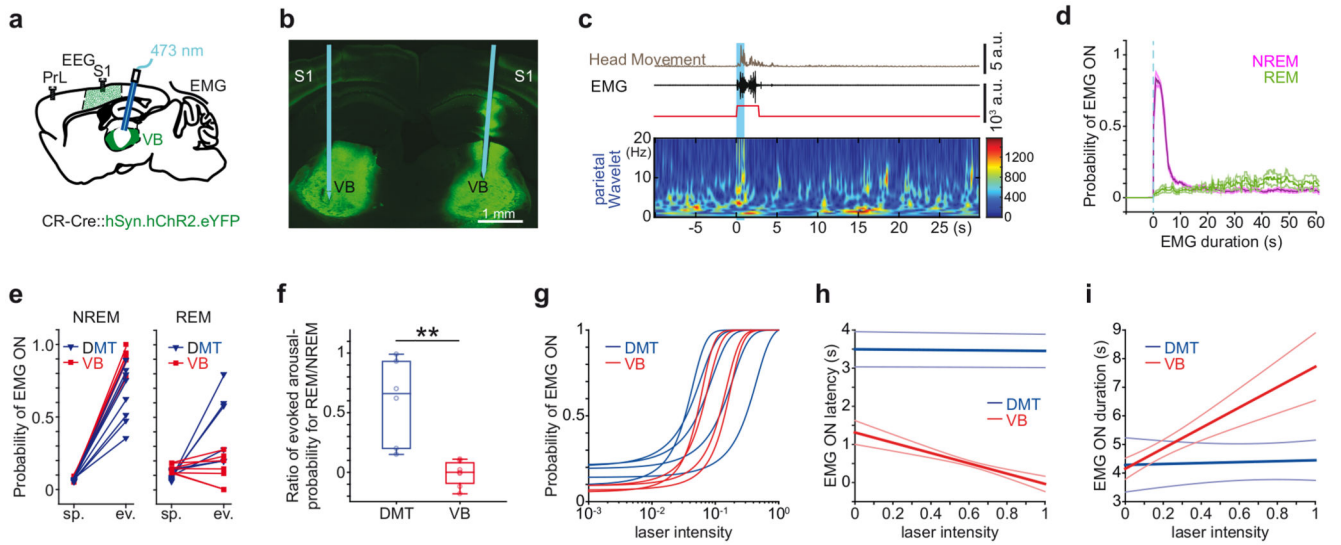
Figure 4. Microarousals evoked by DMT/CR+ cells and sensory nuclei

a, Schematic diagram for the experimental settings.

b, Position of the optic fiber in a coronal section of VB expressing ChR2-eYFP.

c, Microarousal during NREM (left) evoked by 1 sec long stimulation of VB cells.

d, Average (mean) peri-event distribution of EMG ON states shows high probability during NREM (purple; 0.91 ± 0.07, n = 7 unilateral stimulation from 4 mice). VB stimulation was ineffective in REM sleep (green) in response to 1 sec stimulation (blue dashed line). Shaded area represents ± s.e.m.

e, Spontaneous and evoked rate of microarousal induced by 1 sec stimulation of DMT/CR+ (blue) or VB (red) in NREM (left) and REM (right) sleep.

f, Arousal probability in REM normalized to arousal probability in NREM for DMT/CR+ (blue) and VB mice (red). (VB, n = 7; DMT, n = 6; 2*one-tailed Mann-Whitney, p = 0.0011). The horizontal lines in the box plots indicate medians, the box limits indicate first and third quantiles, and the vertical whisker lines indicate minimum and maximum values. The whiskers extend to the most extreme data points.

g, Correlation of laser intensity and arousal probability. Sigmoid was fitted for each animal. To enable comparison of sigmoid slopes between groups, both laser intensities and arousal probabilities were normalized to their maximal values within each mouse. The slope of sigmoid curves showed individual variability, but on average, there was no significant difference between VB and DMT/CR+ animals (VB, n = 4, DMT n = 5 mice; 2*one-tailed Mann-Whitney, p = 0.142).

h, Correlation of laser intensity vs. microarousal latency. dMT-latency: r = -0.05+-0.11; p: n.s in n= 4/5 animals, individual p values: p = 0.023; p = 0.371; p = 0.476; p = 0.57; p = 0.476; VB latency: r = -0.275+-0.09, n= 4 hemisphers, individual p values: p = 0.0028; p = 0.0005; p = 0.0001; p = 0.0001.

i, Correlation of laser intensity vs. microarousal duration. DMT duration: r = 0.01+-0.07; p: n.s in n = 5 animals; individual p values: p = 0.28; p = 0.35; p = 0.59; p = 0.60; p = 0.85. VB-duration: r = 0.2+-0.05; in n = 4 hemispheres, individual p values: p = 0.034; p = 0.001; p = 0.0005; p = 0.0001. Thin blue and red lines represents ± s.e.m.
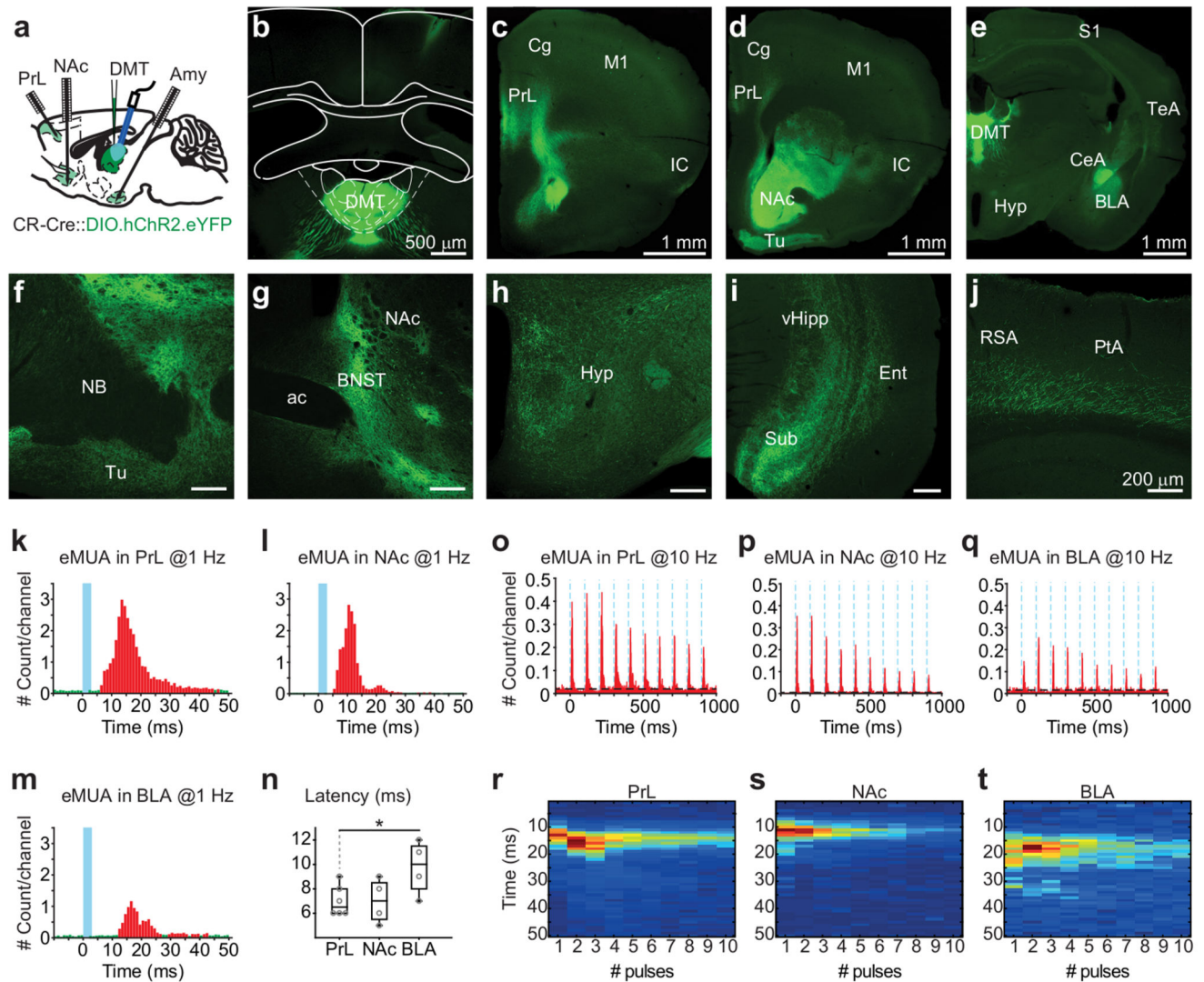
Figure 5. Functional connectivity of DMT/CR+ cells

a, Experimental setting for simultaneous *in vivo* multiunit recordings from three target regions of DMT/CR+.

b-j, Distribution of DMT/CR+ axons in the mouse forebrain. Injection site of AAV-DIO-ChR2-eYFP in DMT of a CR-Cre mouse (in **b**). Similar data were obtained in 29 mice.

k-m, Normalized peri-event time histogram of evoked MUA (eMUA) responses in PrL (**k**), NAc (**l**) and BLA (**m**) at 1 Hz light stimulation of DMT/CR+ (blue line). Bins in red are significantly larger than baseline (green).

n, Population data for latencies of eMUA in PrL (7 ± 1.26 ms, n = 6), NAc (7 ± 1.83 ms, n = 4) and BLA (9.75 ± 2.22 ms; n = 4; two-tailed unpaired *t*-test, PrL vs. BLA, t(8) = -2,526, p = 0.0354).

o-q, Normalized peri-event time histogram of eMUA responses in PrL (**o**), NAc (**p**) and BLA (**q**) at 10 Hz light stimulation (blue dotted lines) of DMT/CR+.

r-t, Normalized heat map showing peak latencies of eMUA at 10 Hz in PrL (**r**), NAc (**s**) and BLA (**t**). The horizontal lines in the box plots indicate medians, the box limits indicate first and third quantiles, and the vertical whisker lines indicate minimum and maximum values. *p < 0.05. ac, anterior commissure; Amy, amygdala; BLA, basolateral amygdala; BNST, bed nucleus of the stria terminalis; CeA, central amygdala; Cg, cingulate cortex; DMT, dorsal medial thalamus; Ent, entorhinal cortex; Hyp, hypothalamus; IC, insular cortex; M1, primary motor cortex; NAc, n. accumbens; NB, nucleus basalis; PrL, prelimbic cortex; PtA; parietal association cortex; RSA, retrosplenial agranular cortex; S1, primary somatosensory cortex; Sub, subiculum; TeA, temporal association cortex; Tu, olfactory tubercle; vHipp, ventral hippocampus.
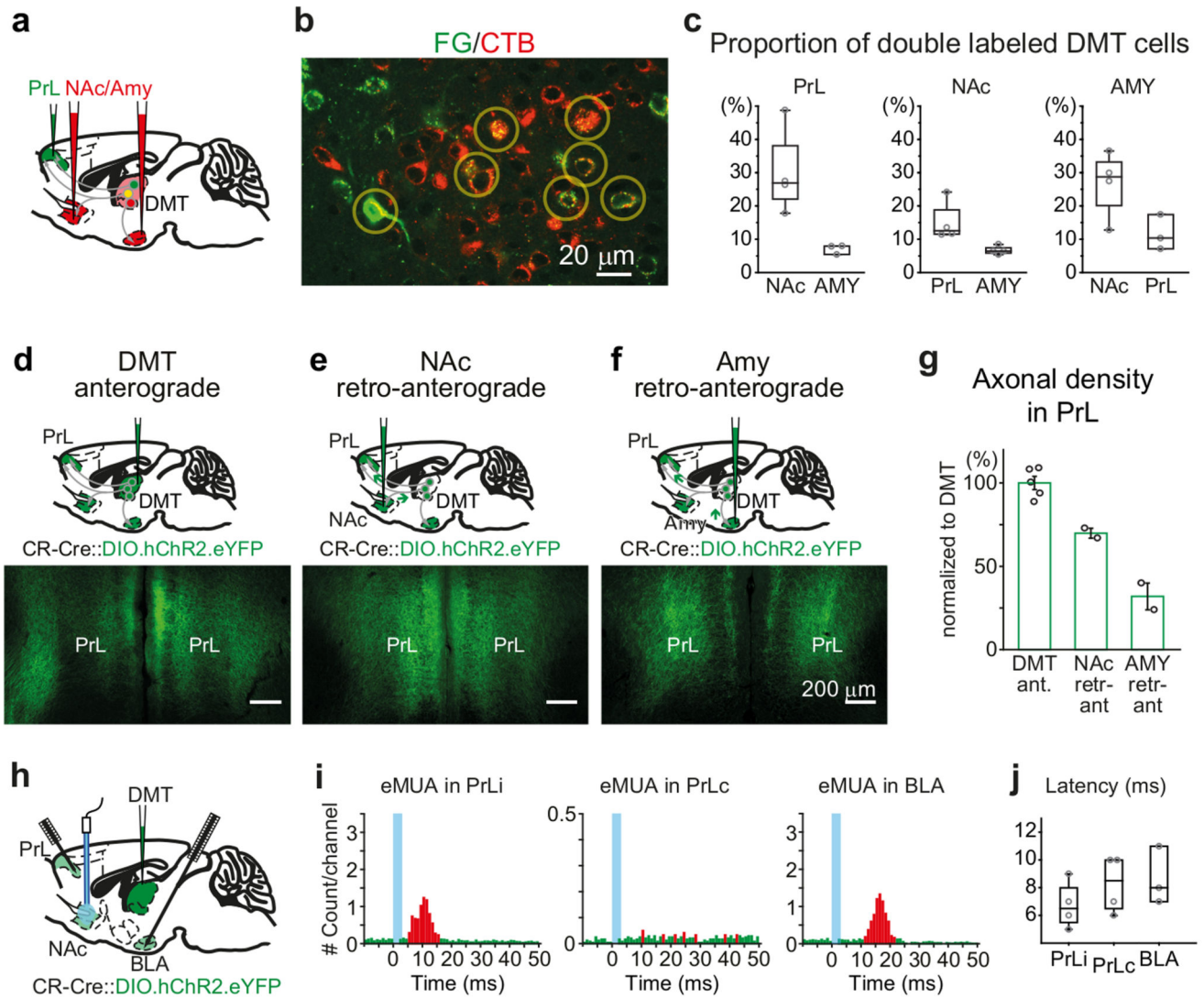
Figure 6. Extensive collateralization of DMT/CR+ cells in multiple forebrain regions

**a**, Experimental design for double retrograde tracings.

b, Confocal fluorescent image of FG (from PrL; green) and CTB (from NAc; red) – labeled thalamic cells in DMT. Yellow circles indicate double-labeled cells.

c, Proportion of PrL- (left), NAc- (middle) and Amy-projecting (right) DMT cells which also project to the other two regions as measured by double retrograde tracing (PrL-AMY, n=3 mice; PrL-NAc, n=4; AMY-NAc; n=4).

d-f, Schematic drawing (top) and representative confocal images (bottom) of DMT/CR+ axonal arbors in PrL obtained by direct, anterograde virus labeling from DMT (**d**) or after injecting the virus to NAc (**e**) and AMY (**f**) utilizing retro-anterograde transport of the viral particles.

g, Population data of the length of DMT/CR+ axon arbors in PrL after direct anterograde labeling from the DMT (DMT Ant; n = 5 mice) or after retro-anterograde labeling from NAc (NAc retr-ant; n = 2 mice) or AMY (AMY retr-ant, n = 2 mice).

h, Experimental design for *in vivo* anesthetized multiunit recording and antidromic optogenetic stimulation.

i, Antidromic stimulation of DMT/CR+ fibers in NAc evokes antidromic-orthodromic multi-unit activations (eMUA) in ipsilateral PrL (iPrL) and BLA but not in the contralateral PrL (cPrL). Blue lines indicate optogenetic stimulation, red/green bars represent those bins in which the MUA was significantly elevated/unchanged (respectively) compared to the baseline.

j, Latencies of antidromic-orthodromic eMUA measured in PrLi (6.75 ± 1.7 ms; n = 4 mice), PrLc (8.25 ± 2.1 ms; n = 4 mice) and BLA (8.7 ± 2.1 ms; n = 3 mice) which did not differ from the direct orthodromic eMUA (two-tailed paired *t*-test, PrL, t(8) = 0,268, p = 0.7957; BLA, t(5) = 0,655, p = 0.5411). Bar graphs are means ± SD; the horizontal lines in the box plots indicate medians, the box limits indicate first and third quantiles, and the vertical whisker lines indicate minimum and maximum values.
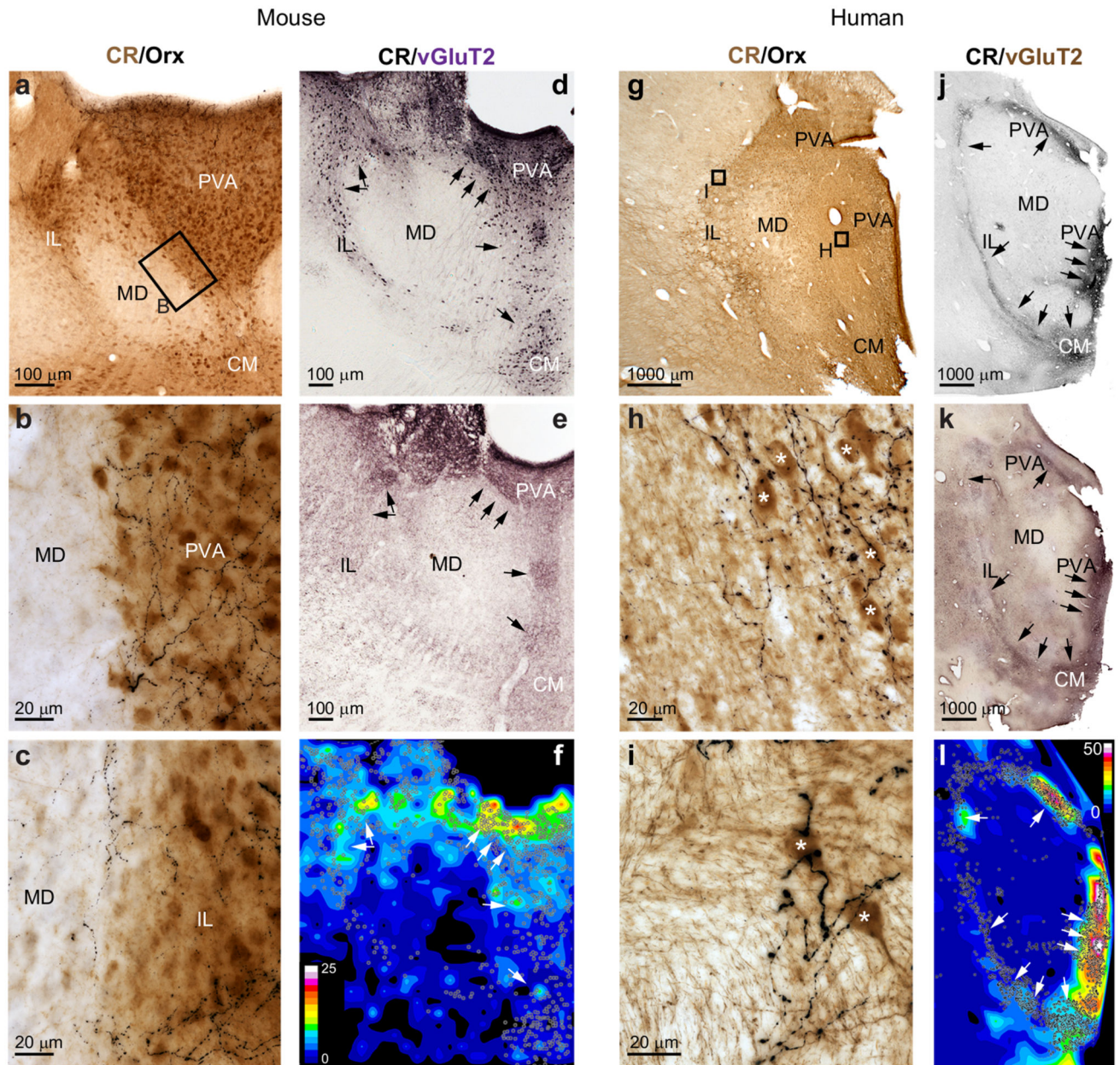
Figure 7. Selective subcortical innervation of DMT/CR+ cells in mice and human.
a, Low-power double immunostaining of mouse DMT for CR (brown) and orexin (Orx, black) (n = 4 mice). Small box represents the enlarged area in **b**.

b-c, High power images from the midline (**b**) and intralaminar (**c**) regions. Note that the orexin-positive fibers are restricted to regions populated by CR+ cells.

d-e, Low power immunostaining for CR (**d**) and vGluT2 (**e**) of the mouse DMT. **f**, Heat-map representing staining density shows large overlap between vGlut2 terminals and the position of CR+ cell bodies in the midline and dorsal intralaminar region.

g-i, Same images as **a-c** in the human thalamus (n = 4 humans). Small boxes indicate the position of high power images.

j-l, Same images as **d-f** in the human thalamus. Scale of the density map: 0-25 bouton/1000 μm^2 (mouse) and 0-50 bouton/1000 μm^2 (human). CM, central Medial thalamic nucleus; IL, intralaminar thalamic nuclei; MD, mediodorsal thalamic nuclei; PVA, paraventricular thalamic nucleus, anterior part.